Chemical Geology 409 (2015) 28–41

Contents lists available at ScienceDirect

Chemical Geology

journal homepage: www.elsevier.com/locate/chemgeo

Monazite response to ultrahigh-pressure subduction from U–Pb dating by laser ablation split stream

Bradley R. Hacker [a,*], Andrew R.C. Kylander-Clark [a], Robert Holder [a], Torgeir B. Andersen [b], Emily M. Peterman [c], Emily O. Walsh [d], Jonathan K. Munnikhuis [e]

[a] Earth Science, University California, Santa Barbara, CA 93106-9630, USA
[b] University of Oslo, Physics of Geological Processes, PO Box 1048, Blindern, 0316 Oslo, Norway
[c] Earth and Oceanographic Science, Bowdoin College, 6800 College Station, Brunswick, ME 04011, USA
[d] Geology, Cornell College, Mount Vernon, IA 52314, USA
[e] Geological Sciences, University of North Carolina, Chapel Hill, Campus Box #3315 Chapel Hill, NC 27599-3315, USA

ARTICLE INFO

Article history:
Received 5 February 2015
Received in revised form 6 May 2015
Accepted 11 May 2015
Available online 22 May 2015

Editor: K. Mezger

Keywords:
Monazite
Laser ablation
Split stream
Petrochronology

ABSTRACT

To assess the response of monazite during subduction of continental crust to mantle depths, U–Pb isotopic ratios and elemental abundances were measured simultaneously by laser-ablation split-stream inductively-coupled plasma mass spectrometry (LASS) in rocks from the ultrahigh-pressure Western Gneiss Region of the Scandinavian Caledonides. Nearly seventy different samples of quartzofeldspathic basement and overlying metasedimentary rocks were studied. Pre-subduction monazite (chiefly 1.6 Ga and 1.0 Ga) is preserved locally in the structurally lowest, basement rocks because earlier, Precambrian tectonism produced coarse-grained, high-grade rocks that were resistant to further recrystallization in spite of syn-subduction temperatures and pressures of 650–800 °C and 2–3.5 GPa. A few of the monazite in the metasedimentary rocks atop the basement preserve syn-subduction U–Pb dates, but the majority continued to recrystallize during post-subduction exhumation and record a general westward decrease in age related to westward-progressing exhumation. The absence of Precambrian monazite in the metasedimentary rock atop the basement suggests that sedimentation postdated the 1.0–0.9 Ga high-grade metamorphism and was late Proterozoic to early Paleozoic.

1. Introduction

The development of techniques to analyze monazite U/Th–Pb dates in situ by electron probe [Suzuki et al., 1991], SIMS [Harrison et al., 1995], and LA-ICP-MS [Kosler et al., 2001] has spurred renewed interest in the petrogenesis of monazite, including understanding neocrystallization [Kingsbury et al., 1993], recrystallization [Finger, 1998], composition [Franz et al., 1996], and thermometry [Gratz and Heinrich, 1997; Pyle et al., 2001]. Advances in these complementary tracks of analytical methods and petrologic interpretation have enabled increasing use of monazite as a petrochronometer—i.e., the interpretation of isotopic dates in the context of elemental or complementary isotopic information collected from the same mineral.

One might infer from recent models [Kelsey, 2008] [Yakymchuk and Brown, 2014] that monazite is routinely recrystallized during high-temperature orogenesis and that its U–Pb age records only the final, cooling stage. Here we apply LASS (laser-ablation split-stream inductively-coupled plasma mass spectrometry) [Kylander-Clark et al., 2013] to monazite from the ultrahigh-pressure (UHP) Western Gneiss Region (WGR). Our objective in using in situ, combined U–Pb and trace-element analysis of monazite is to understand the broad-scale metamorphic response of monazite and its host rocks during subduction to, and exhumation from, UHP conditions. The premise behind collecting trace-element and isotopic data simultaneously is that the trace elements provide insight into the petrological context of the isotopic dates: depressed heavy rare earth element concentrations may indicate that an interpreted U–Pb date coincides with the stability of garnet [Rubatto, 2002], elevated Eu and Sr may indicate HP recrystallization and plagioclase instability [Finger and Krenn, 2007; Holder et al., 2015], and Th and U help understand fluid availability [Hoskin and Schaltegger, 2003] and its potential role in monazite recrystallization [Seydoux-Guillaume et al., 2002]. We show that some monazite survived amphibolite–granulite-facies metamorphism, partial melting, and subduction with its original age intact.

2. Geologic setting

The Western Gneiss Region (WGR) of Norway contains one of Earth's largest ultrahigh-pressure terranes (Fig. 1). Like most well-exposed and extensively investigated UHP terranes, the WGR is dominated by quartzofeldspathic gneiss; eclogite and (U)HP

* Corresponding author. Tel.: +1 805 893 7952.
E-mail address: hacker@geol.ucsb.edu (B.R. Hacker).

http://dx.doi.org/10.1016/j.chemgeo.2015.05.008
0009-2541/

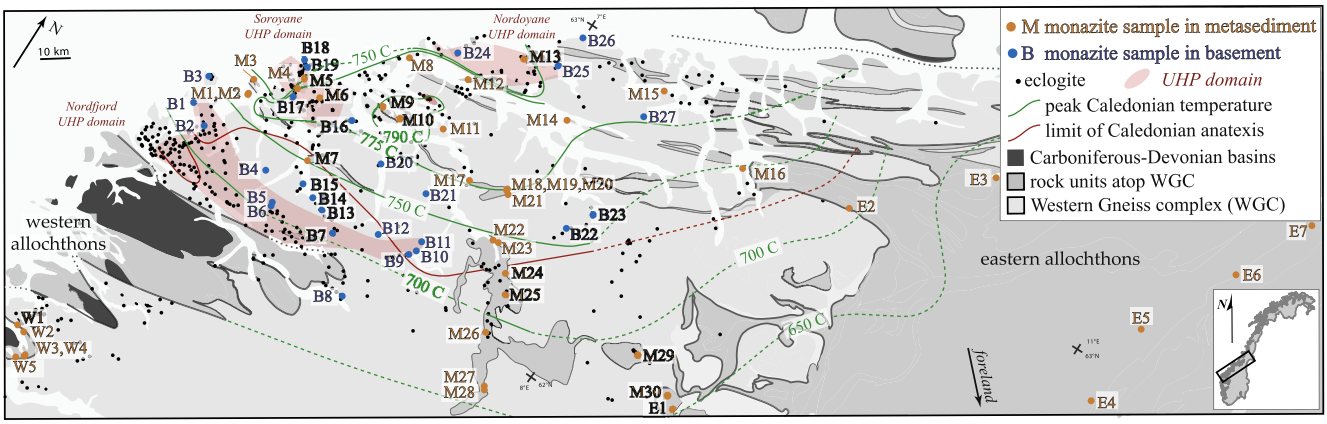

Fig. 1. Map of the Western Gneiss Region, including western allochthons, eastern allochthons, and metasedimentary rocks atop the Western Gneiss complex. Eclogites are widespread; UHP domains concentrated in core of orogen. Exhumation-related temperatures generally increase northwestward from 600 °C to 800 °C (green). (For interpretation of the references to color in this figure legend, the reader is referred to the web version of this article.)

peridotite comprise only a few volume percent of the Region. The quartzofeldspathic gneiss and eclogite protoliths formed chiefly by magmatism at ~1.68–1.64 Ga, 1.29–1.24 Ga, and ~990–950 Ma [Corfu and Andersen, 2002; Walsh et al., 2007; Krogh et al., 2011; Corfu et al., 2013]; regional metamorphism [Roffeis and Corfu, 2014] associated with the ~1.0–0.9 Ga magmatism reached temperatures of ~775–825 °C [Spencer et al., 2013]. During the Caledonian orogeny, subduction-related magmatism related to closure of the Iapetus ocean ended at ~430 Ma [Corfu et al., 2006], marginal basin ophiolites and island arcs were emplaced onto the Baltica craton in the Wenlock [Andersen et al., 1990], and the previously hyperextended continental margin

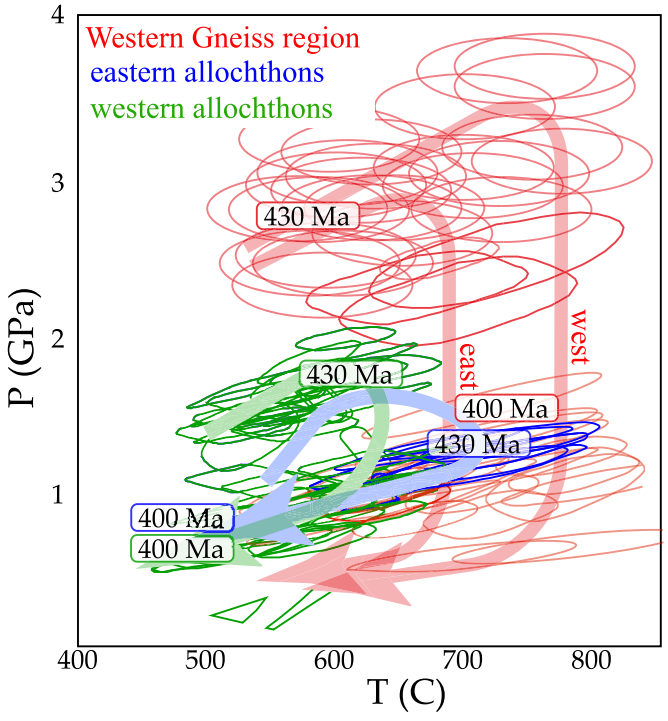

Fig. 2. Beginning at 430 Ma, the WGR (red) was metamorphosed at eclogite-facies conditions of 1.8–3.6 GPa and 650–800 °C, the eastern allochthons (blue) reached 1.2 GPa and 700 °C, and the western allochthons (green) reached 1.6 GPa and 600 °C. Beginning at 400 Ma, exhumation-related overprinting of all these rocks occurred at ~1 GPa at amphibolite-facies temperatures from ~750 °C to 550 °C. (For interpretation of the references to color in this figure legend, the reader is referred to the web version of this article.)
References: Cuthbert et al., 2000; Terry et al., 2000; Hacker et al., 2003; Labrousse et al., 2004; Ravna and Terry, 2004; Walsh and Hacker, 2004; Hacker and Gans, 2005; Root et al., 2005.

[Andersen et al., 2012] began to contract. The combined thrust stack was subducted, and eclogites [Krogh, 1977; Gee, 1980; Andersen et al., 1991; Hacker and Gans, 2005] and (U)HP peridotites formed between ~425 and ~405 Ma [Glodny et al., 2008; Kylander-Clark et al., 2009; Krogh et al., 2011; Beckman et al., 2014; Kylander-Clark and Hacker, 2014].

Eclogite and (U)HP peridotite crop out over an area of ~30,000 km^2 [Hacker et al., 2010], and range in peak metamorphic conditions from ~600 °C and 1.8 GPa near the foreland to ~800 °C and 3.6 GPa (Fig. 2) in the core of the orogen [see geothermometry reported below and summaries in Cuthbert et al., 2000; Ravna and Terry, 2004; Hacker, 2006; Spencer et al., 2013]. Ultrahigh-pressure (UHP) rocks with coesite, diamond, or equivalent metamorphic pressures [e.g., Smith, 1984; Vrijmoed et al., 2008] are restricted to three main domains in the hinterland (pink in Fig. 1). High-pressure Barrovian metamorphism in the allochthons east and west of the WGR reached lower peak PT conditions (~600 °C/1.5 GPa in the western allochthons [Chauvet et al., 1992; Hacker et al., 2003; Johnston et al., 2007b], and ~750 °C/1.3 GPa in the eastern allochthons [Hacker and Gans, 2005]) at roughly the same time (Fig. 2).

Within the area of Fig. 1, there are two main rock units: the structurally lower Western Gneiss Complex (WGC)[1] (pale gray in Fig. 1), and overlying lithologically more-diverse rocks (dark gray in Fig. 1). The WGC is dominated by quartzofeldspathic gneiss, but includes minor amounts of other rock, most notably eclogite and (U)HP peridotite. The overlying rocks are distinguished by a greater abundance of metasedimentary rock—metapelite, carbonate, quartzite—plus amphibolite, eclogite and quartzofeldspathic gneiss. In the eastern part of Fig. 1 ("eastern allochthons"), these rocks are dominant and demonstrably allochthonous [Roberts and Gee, 1985]. Extensive areas of similar rocks in the western part of Fig. 1 ("western allochthons") are also inferred to be allochthonous [Bryhni, 1989] [but see, Tillung, 1999]. Further, smaller outcrops of similar rocks crop out across the rest of the WGR; some may be equivalent to the allochthons to the west and east [Hernes, 1956; Rickard, 1985; Bryhni, 1989; Robinson, 1995; Terry et al., 2000; Tucker et al., 2004; Walsh and Hacker, 2004; Root et al., 2005; Young et al., 2007], and some may be autochthonous sediment deposited on the basement [Schouenborg, 1988; Swensson and Andersen, 1991; Tillung, 1999]. Strong deformation and metamorphism make distinguishing between these two possibilities difficult; herein we refer to all of the metasedimentary rocks that overlie the

[1] Western Gneiss Region refers to the gneiss-dominated area between the eastern and western allochthons. Western Gneiss *Complex* refers to the basement gneiss within the Western Gneiss Region, distinct from allochthonous rocks in the same area.

WGC in the central part of Fig. 1 as 'metasediments' for simplicity, regardless of whether they are allochthonous or autochthonous.

Most of the rocks in the area of Fig. 1 are amphibolite to granulite facies. In the WGR they record chiefly Barrovian peak metamorphic conditions of ~650–800 °C and ~1 GPa (Fig. 2) [Terry et al., 2000; Hacker et al., 2003; Labrousse et al., 2004; Walsh and Hacker, 2004; Root et al., 2005; Johnston et al., 2007a; Spencer et al., 2013; Fauconnier et al., 2014]. This was accompanied by partial melting that was locally extensive in the hinterland, but progressively more feeble toward the foreland [Ganzhorn et al., 2014] [Hacker et al., 2010 #5959] [Kylander-Clark and Hacker, 2014].

U–Pb zircon, U–Pb titanite, Sm–Nd garnet, and $^{40}Ar/^{39}Ar$ mica geochronology reveal at least two periods of metamorphism in most of the WGR: one Proterozoic and one Caledonian [Tucker et al., 1987; 1990; 2004; Walsh et al., 2007; Kylander-Clark et al., 2008; Corfu et al., 2013]. In the eastern part of the WGC, metamorphic titanite and garnet are Proterozoic, whereas in the western part titanite and garnet at most locations are Caledonian [Johnston et al., 2007b; Peterman et al., 2009; Spencer et al., 2013]. The end of Caledonian metamorphism is definitively signaled by $^{40}Ar/^{39}Ar$ muscovite dates of 425–405 Ma in the eastern allochthons, 440–395 Ma in the western allochthons, and 400–380 Ma from east to west across the WGR (Fig. 1) [Hacker and Gans, 2005; Walsh et al., 2007; Young et al., 2011; Walsh et al., 2013]; these are inferred to record westward-propagating exhumation of the Western Gneiss Region [Walsh et al., 2013]. Exhumation was accompanied by melting from 400 to 385 Ma [Austrheim et al., 2003; Gordon et al., 2013; Ganzhorn et al., 2014], with the youngest and most-extensive melting along the western edge of the WGR [Spencer et al., 2013; Kylander-Clark and Hacker, 2014].

Aside from K-white mica dates, the rocks in the metasediments atop the WGC are largely undated. They contain local eclogite, implying that they were subducted during the Caledonian. We do not know, however, whether most of the metasediments were also metamorphosed in the Precambrian (e.g., ca. 1 Ga) and/or during the Phanerozoic prior to subduction (e.g., 460 Ma). In this paper we show that the monazite-bearing metasedimentary rocks in the metasediments contain Caledonian monazite only, and no sign of an earlier, Precambrian event. We therefore suggest that much of the sediments atop the WGR in Fig. 1 are post-Sveconorwegian or lower Paleozoic [but see, Røhr et al., 2004].

3. Analytical methods

In this study we targeted monazite in the basement gneiss, in metasediments, and in the allochthons to assess how monazite responded during UHP subduction. We analyzed sixty-nine samples by LASS (laser-ablation split-stream inductively coupled-plasma mass spectrometry), including the six previously described by Holder et al. [2015]. Fig. 3 and Table 1 summarize the data. Sample descriptions and graphical depictions of the data for all samples are presented in Supplementary Fig. 1, and the complete U–Pb and trace-element data are available in Supplementary Table 1.

All the samples were analyzed in thin section so that the monazite U–Pb dates and trace-element abundances could be tied to metamorphic textures and parageneses. Each was imaged using back-scattered electrons and/or X-rays on the Cameca SX-100 electron microprobe at UCSB. Samples were ablated using a Photon Machines 193 nm ArF excimer ultraviolet laser with a HelEx ablation cell coupled to a Nu Instruments Plasma high-resolution multi-collector inductively coupled plasma mass spectrometer (MC-ICPMS) and either a Nu Instruments AttoM high-resolution single-collector ICP or an Agilent 7700S quadrupole ICPMS. The laser spot diameter was 10 μm and the laser fluence was ~1 J/cm^2. The laser was fired twice to remove common Pb from the sample surface and this material was allowed to wash out for 10 s. Material was then ablated at 3 Hz for 20 s, resulting in a pit depth of ~6 μm. On the Plasma, masses $^{204}Pb + Hg$, ^{206}Pb, ^{207}Pb, and ^{208}Pb were measured on ion counters, and masses ^{232}Th and ^{238}U were measured on Faraday detectors. Elemental data collection on the AttoM was done in semi-quantitative mode. Analyses of unknowns were bracketed by analyses of the monazite reference materials (RM) 44069 [424.9 Ma $^{207}Pb/^{235}U$ TIMS age, Aleinikoff, 2006] and Bananeira (supplied by Richard Stern) [509 Ma $^{206}Pb/^{238}U$ ICP age, Kylander-Clark et al., 2013; Palin et al., 2013]; 44069 was used as the primary RM for U–Pb analyses and Bananeira was used as the primary RM for trace-element analyses. Additional monazite reference materials 554 [45 Ma $^{208}Pb/^{232}Th$ age, Harrison et al., 1999] [45.6 Ma $^{207}Pb/^{235}U$ CA-TIMS age, Peterman et al., 2012], FC [55.7 Ma Pb/U TIMS age, Horstwood et al., 2003], Trebilcock [272 Ma $^{207}Pb/^{235}U$ TIMS age, Tomascak et al., 1996], and Manangotry [555 Ma J. Cottle personal communication, Horstwood et al., 2003] were included as further monitors of accuracy.

The Iolite plug-in v. 2.5 (Paton et al., 2011) for the Wavemetrics Igor Pro software was used to correct measured isotopic ratios for baselines, time-dependent laser-induced inter-element fractionation, plasma-induced fractionation, and instrument drift. Baseline intensities were determined prior to each analysis. The mean and standard error of the measured ratios of the backgrounds and peaks were calculated after rejection of outliers more than 2 standard errors beyond the mean.

The uncertainty of individual measurements is dominated by counting statistics and signal stability. The $^{207}Pb/^{206}Pb$ measurements require up to 2% additional external error attributable either to variation in ablation or transport characteristics; this was added in quadrature.

The $^{238}U/^{206}Pb$ and $^{207}Pb/^{206}Pb$ isotopic ratios for each analysis were plotted on Tera-Wasserburg (1972) diagrams using Isoplot (Ludwig,

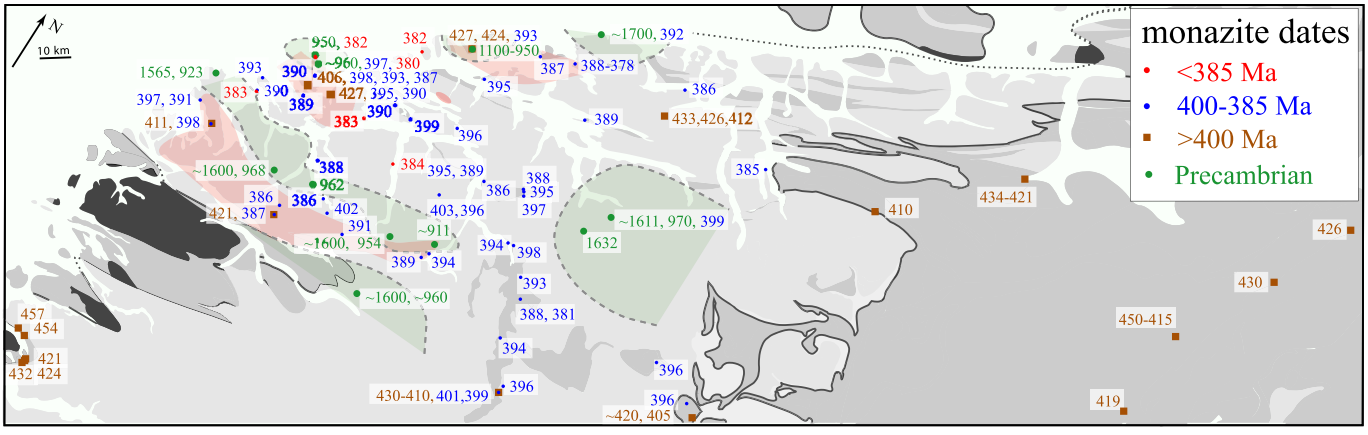

Fig. 3. Geologic map with monazite dates. Domains with Precambrian dates shaded green. Pre-subduction and syn-subduction dates in brown; most are in allochthons, but also local in WGR. Syn-exhumation dates in blue; youngest are red. Unit names and symbols same as Fig. 1. (For interpretation of the references to color in this figure legend, the reader is referred to the web version of this article.)

Table 1
Summary of monazite data.

Sample name	Geologic unit	Group	Mineralogy	Texture	Monazite size (μm)	Zoning	Date (Ma)	±2σ	UTM N (zone 32 V)	UTM E	IGSN	Original name
E1	Blåhø	E.A.	GM	B/P	10	Homo.	420	12	6894501	0495677	IEBRH0001	E9731H5
E1	Blåhø	E.A.	GM	B/P	10	Homo.	405	4.2	6894501	0495677		E9731H5
E2	Blåhø	E.A.	GBM	A	20–50	Patchy	410	1.1	6984251	0507598	IEBRH0002	H1604E4
E3	Gula	E.A.	GStBM	A	10–20	Patchy	434–421		7022500	0545400	IEBRH0003	H1604J2
E4	Gula	E.A.	KGSBM	G	10	Homo.	419	6.5	6972866	0612396	IEBRH0004	H1603N3
E5	Gula	E.A.	GBM	B & G	10–15	Homo.	450–415		7004747	0612416	IEBRH0005	H1602A1
E6	Gula	E.A.	KGSB	P & G	15–20	Patchy	430	3.3	7038262	0629134	IEBRH0006	H1531B1
E7	Gula	E.A.	GBM	P & G	10–20	Patchy	426	3.4	7066811	0642868	IEBRH0007	H1601D1
W1	Hyllestad	W.A.	KGSBM	B/P	15–100	N/a	457	2.5	6794041	0293277	IEBRH0008	V0805J
W2	Hyllestad	W.A.	KGSBM	G, B/P	200	Patchy	454	1.5	6793423	0296490	IEBRH0009	V9825F
W3	Hyllestad	W.A.	KGSMPa	G P	15–40	Homo.	421	1.6	6786651	0301273	IEBRH000A	V9818I
W4	Hyllestad	W.A.	KGM	G, B/P	15–40	n/a	424	0.7	6786651	0301273	IEBRH000B	V9818I7
W5	Hyllestad	W.A.	KGSBM	G & mica	50–200	Homo.	432	4.2	6786651	0301273	IEBRH000C	V9818I9B
M1	ms w. ec	single	KGBM	B	20	Homo.	383	1.1	6902980	0315910	IEBRH000D	8907C1
M2	ms w. ec	single	KGSBSi	B	20	Homo. or Y rims	390	1.3	6902980	0315910	IEBRH000E	8907C7
M3	ms w. ec	single	KGSBC	B/P	25–50	Y rims	393	1.1	6908472	0313872	IEBRH000F	R9828C30
(H) M4	ms w. ec	multi	KGBM	Porphyroblast	400	Sector	**406**	3.3	6911450	0327705	IEBRH000G	8828A5
(H) M4	ms w. ec	multi	KGBM	Porphyroblast	400	Homo.	398	2.7	6911450	0327705		8828A5
(H) M4	ms w. ec	multi	KGBM	Porphyroblast	400	Homo.	393	0.6	6911450	0327705		8828A5
(H) M4	ms w. ec	multi	KGBM	Porphyroblast	400	Y rims	387	1.4	6911450	0327705		8828A5
M5	ms w. ec	single	KGB	B	10	Homo.	390	1.5	6919200	0319200	IEBRH000H	8830A16
(H) M6	ms w. ec	multi	KGBSi	B, apatite	10–60	Patchy; Y-rich rims	**427**	5.6	6916292	0335577	IEBRH000I	R9823A2
(H) M6	ms w. ec	multi	KGBSi	B, apatite	10–60	Patchy; Y-rich rims	395	1.2	6916292	0335577		R9823A2
(H) M6	ms w. ec	multi	KGBSi	B, apatite	10–60	Patchy; Y-rich rims	390	2.1	6916292	0335577		R9823A2
M7	ms	single	KGB	B	10	Homo.	388	3.2	6896496	0344698	IEBRH000J	E1612A
M8	ms w. ec	single	KGB	G, B	20	Homo. or Y rims	382	1.2	6945073	0354946	IEBRH000K	A0721H2
M9	ms	single	KGB	B, P	20–50	Homo. & Y rim	390	0.9	6926531	0355852	IEBRH000L	K1729E1
M10	ms	single	KGSB	B	20	n/a	399	1.7	6926483	0363806	IEBRH000M	A0720H
M11	ms	single	BMSiMa	B/P	20–50	Y-rich cores	396	0.9	6930863	0377457	IEBRH000N	R9821C2
M12	ms	single	GB	B/apatite	50–100	Homo. or Y rims	395	0.8	6947900	0373000	IEBRH000O	G9707B1
M13	ms w. ec	single	KGB	B/P	5–20	Homo.	387	2.1	6966304	0387703	IEBRH000P	G9708R3
M14	ms	single	GStB	B/P, A	20–30	n/a	389	1.3	6956367	0411568	IEBRH000Q	K3806B1
M15	ms	single	KGB	Mica/P	20–60	Patchy & Y cores	386	1.3	6982003	0433024	IEBRH000R	K1801G3
M16	ms	single	GBM	B/P	10–20	Homo.	385	4.9	6975204	0469937	IEBRH000S	K1731P1
M17	ms w. ec	single	GB	B/P	10–50	n/a	386	2.1	6920746	0393801	IEBRH000T	E9806B1
M18	ms	single	GKBSi	B or P	5–20	Homo.& Y rims	395	1.2	6925820	0407525	IEBRH000U	P5703B1
M19	ms	single	GB	B or B/P	10–40	Homo.& Y rims	394	1.3	6925820	0407525	IEBRH000V	P5703B3
M20	ms	single	KGB	B/P	10–40	Y rims	388	2.2	6925820	0407525	IEBRH000W	P5703B4
M21	ms	single	KGB	B/P	10–40	Homo. or Y rims	397	2.3	6826222	0408438	IEBRH000X	E1622F2
M22	ms	single	GMBSiX	B/P	20–30	Y rims	394	1.3	6908065	0412007	IEBRH000Y	E9804J1
M23	ms	single	GMBSi	Mica/P	20–50	Homo. or Y rims	398	1.7	6907756	0414173	IEBRH000Z	E9804K5
M24	ms w. ec	single	GBM	B	20–60	Patchy	393	1.8	6898077	0420386	IEBRH0010	E1614c
M25	ms	single	KGB	B or B/P	10–20	Patchy	388	3.1	6894654	0426458	IEBRH0011	P5711C
M26	ms w. ec	single	KGSB	B & B/apatite	10–50	Homo.	394	1.4	6879216	0427149	IEBRH0012	E9819D1
M27	ms w. ec	single	GBM	B/P	20–100	Patchy	396	1.3	6864668	0436977	IEBRH0013	E9817Gb2
(H) M28	ms w. ec	multi	KGSBSi	B	40–60	Homo.& Y rims	**430–410**		6864668	0436977	IEBRH0014	E9817G8
(H) M28	ms w. ec	multi	KGSBSi	B	40–60	Homo.& Y rims	401	2.7	6864668	0436977		E9817G8
(H) M28	ms w. ec	multi	KGSBSi	B	40–60	Homo.& Y rims	399	2.3	6864668	0436977		E9817G8
M29	ms w. ec	single	KGSBX	B/P	20–40	n/a	396	1.1	6902671	0475158	IEBRH0015	M8713A2
M30	ms	single	GBM	B near apatite	10	Homo.	396	4.3	6896386	0492058	IEBRH0016	E9731D2
B3	WGC w. ec	Pc	GBM	B, P, G	40–100	Patchy	1565	19	6901461	0300727	IEBRH0019	P6806E2
B3	WGC w. ec	Pc	GBM	B, P, G	40–100	Patchy	923	6	6901461	0300727		P6806E2
B4	WGC	Pc	GBMSi	Mica, P	20–40	Oscillo. & homo.	~1600		6885870	0334890	IEBRH001A	P6822B3
B4	WGC	Pc	GBMSi	Mica, P	20–40	Oscillo. & homo.	968	7	6885870	0334890		P6822B3
B8	WGC w. ec	Pc	GBM	P	35	n/a	~1600	n/a	6863444	0379741	IEBRH001E	E9809O2
B8	WGC w. ec	Pc	GBM	P	35	n/a	~960		6863444	0379741		E9809O2
B11	WGC	Pc	GB	B	20–60	Homo.	911	11	6893424	0391896	IEBRH001H	E1613E1
B12	WGC w. ec	Pc	GBSiMa	B, P, G	20–60	Y cores	~1600		6888574	0379031	IEBRH001I	K1725B2
B12	WGC w. ec	Pc	GBSiMa	B, P, G	20–60	Y cores	954	5	6888574	0379031		K1725B2
B15	WGC w. ec	Pc	GBSiM	P	15, 200	Homo.	962	13	6888850	0347440	IEBRH001L	P5626G1
B1	WGC w. ec	multi	GBM	Mica	15–60	Homo. & Y rims	397	1.7	6891321	0302307	IEBRH0017	P6807G3
B1	WGC w. ec	multi	GBM	Mica	15–60	Homo.& Y rims	391	3.0	6891321	0302307	IEBRH0018	P6807G3
(H) B2	WGC w. ec	multi	HB	Porphyroblast	100–200		**411**	1.7	6971337	0432409		8910A3
(H) B2	WGC w. ec	multi	HB	Porphyroblast	100–200		398	1.1	6971337	0432409		8910A3
B6	WGC w. ec	multi	KGBSi	Mica/P	20–60	Patchy	**421**	3	6877781	0341890	IEBRH001C	K1727B1
B6	WGC w. ec	multi	KGBSi	Mica/P	20–60	Patchy	387	1.5	6877781	0341890		K1727B1
B19	WGC	multi	GBSi	G, B/P	10–30	n/a	397	3.2	6923822	0325833	IEBRH001P	R9824B3
B19	WGC	multi	GBSi	G, B/P	10–30	n/a	380	2.8	6923822	0325833		R9824B3
B19	WGC	multi	GBSi	G, B/P	10–30	n/a	~930		6923241	0327304		R9824B3
B21	WGC	multi	BMSiX	B/P	40–300	Y rims	403	3.4	6908403	0384433	IEBRH001R	E9808D6
B21	WGC	multi	BMSiX	B/P	40–300	Y rims	396	3.4	6908403	0384433		E9808D6
(H) B24	WGC?	multi	KGB	G	20–40	Homo.	**427**	1.7	6956155	0366055	IEBRH001U	H3630B2
(H) B24	WGC?	multi	KGB	G	20–40	Homo.	**424**	3.0	6956155	0366055		H3630B2

(continued on next page)

Table 1 (*continued*)

Sample name	Geologic unit	Group	Mineralogy	Texture	Monazite size (μm)	Zoning	Date (Ma)	±2σ	UTM N (zone 32 V)	UTM E	IGSN	Original name
(H) B24	WGC?	multi	KGB	G	20–40	Homo.	393	3.3	6956155	0366055		H3630B2
B27	WGC	multi	KGB	G & G/P	20–40	n/a	**433**	3.0	6971337	0432409	IEBRH001X	K2711E1
B27	WGC	multi	KGB	G & G/P	20–40	n/a	**426**	0.9	6971337	0432409		K2711E1
B27	WGC	multi	KGB	G & G/P	20–40	n/a	**412**	2.2	6971337	0432409		K2711E1
B27	WGC	multi	KGB	G & G/P	20–40	n/a	~1200		6971337	0432409		K2711E1
B18	WGC	Pc/Caled	KGB	B/P	20–250	Oscillo. & homo.	950	14	6923822	0325833	IEBRH001O	R9823I8
B18	WGC	Pc/Caled	KGB	B/P	20–250	Oscillo. & homo.	382	2.4	6923822	0325833		R9823I8
B22	sill gneiss	Pc/Caled	BMSiX	B/P	20–30	Hi & low Y rims	1632	14	6925587	0431115	IEBRH001S	E9804C3
B22	sill gneiss	Pc/Caled	BMSiX	B/P	20–30	hi & low Y rims	Caledonian		6925587	0431115		E9804C3
B23	sill gneiss	Pc/Caled	BSi	P	30–100	Oscillo. & homo.	1611	7	6934179	0435001	IEBRH001T	E1616A
B23	sill gneiss	Pc/Caled	BSi	P	30–100	Oscillo. & homo.	970	12	6934179	0435001		E1616A
B23	sill gneiss	Pc/Caled	BSi	P	30–100	Oscillo. & homo.	399	3.4	6934179	0435001		E1616A
(H) B24	WGC?	Pc/Caled	KGB	G	20–40	Homo.	950–1100		6956155	0366055		H3630B2
B26	WGC	Pc/Caled	KGBM	B/P	20–50	Oscillo. & homo.	392	1.5	6983190	0400451	IEBRH001W	K1801S1
B26	WGC	Pc/Caled	KGBM	B/P	20–50	Oscillo. & homo.	~1700		6983190	0400451		K1801S1
B5	WGC w. ec	single	KGBM	Mica/P	10–50	Patchy	386	1.6	6876955	0341170	IEBRH001B	K1727H1
B7	WGC w. ec	single	GBX	B/P	10–50	Homo.	391	1.5	6881248	0364999	IEBRH001D	K1726G2
B9	WGC w. ec	single	BMSi	Mica	40–100	Patchy & Y rims	389	1.1	6886907	0389440	IEBRH001F	E1613A9
B10	WGC w. ec	single	BM	P/apatite	30–60	Patchy	394	0.9	6890278	0391713	IEBRH001G	E9809C7
(H) B13	WGC w. ec	single	GBSiM	B	10, 100	Homo.& sector?	402	0.7	6884567	0357559	IEBRH001J	P5624E
B14	WGC w. ec	single	GBM	Mica/P	20–80	Patchy & Y rims	386	0.6	6886451	0352345	IEBRH001K	P5624A3
B16	WGC w. ec	single	GBSi	B	20	n/a	383	1.1	6915663	0349283	IEBRH001M	A0804G5
B17	WGC	single	M		Grain separate		389	2.0	6911566	0328833	IEBRH001N	P5701A5
B20	WGC w. ec	single	GB	B/P	10–20	Homo.	384	1.2	6909234	0366201	IEBRH001Q	E9814A5
B25	sill gneiss	single	GBSi	B	20–150	Patchy	383	1.2	6970946	0398970	IEBRH001V	J5815E4

Sample name. "(H)" indicates sample from Holder et al. [2015].
Geologic unit: "ec" eclogite; "ms" metasedimentary rock atop WGC; "sill" sillimanite; "WGC" Western Gneiss Complex.
Group: "E.A." eastern allochthons; "multi", Western Gneiss region samples with multiple populations of Caledonian monazite; "Pc", Western Gneiss region samples with only Precambrian monazite; "Pc/Caled", Western Gneiss region samples with only Precambrian and Caledonian monazite; "single", Western Gneiss region samples with single population of Caledonian monazite; "W.A.", western allochthons.
Mineralogy & texture: "A" allanite; "B", biotite; "C" cordierite; "G" garnet; "H" hornblende; "K" kyanite; "M" muscovite; "Ma" margarite; "P" plagioclase; "Pa" paragonite; "S" sillimanite; "S" staurolite; "X" xenotime.
All have feldspar and quartz.
Texture: hosting grain or "/" signifies boundary between two grains.
Date (Ma): U–Pb isochron date from this study. Stated uncertainty includes in-run errors and decay constant errors only. The total uncertainty is a minimum of 2% or 8 Myr for a 400 Ma date.
Bold indicates syn-UHP date.
IGSN, International GeoSample Number.

2003). All date uncertainties are reported at the 95% confidence interval, assuming a Gaussian distribution of measurement errors. For discordant data with a broad spread of U–Pb ratios—and thus, a well-constrained common $^{207}Pb/^{206}Pb$ ratio—we report the $^{238}U/^{206}Pb$–$^{207}Pb/^{206}Pb$ isochron date or '207-corrected' date. For discordant data with a small spread of U–Pb ratios—and thus, a poorly constrained common $^{207}Pb/^{206}Pb$ ratio—we anchor the ratio to the Stacey–Kramers (1975) value for common Pb. Holder et al. [2015] showed that this is justified for monazite in this dataset for four reasons, largely because the large number of analyses helps assess the extent to which inheritance and/or common Pb contribute to the discordance. 1) The discordant data are clustered—as though from a common-Pb component of distinct abundance—and not distributed along a discordia line typical of variable inheritance. 2) The discordant data come from distinct compositional domains within the grains. 3) The discordant analyses contain higher concentrations of ^{204}Pb and the Pb composition of biotite in each of his samples was found to be the same as predicted by the Stacey–Kramers model.

The long-term uncertainty in the date of a homogeneous unknown has an uncertainty due to secular variations in the behavior of the laser, the laser-stream transmission, and the ICPMS, and is best estimated from repeat analyses of standards. During the course of this study we obtained $^{206}Pb/^{238}U$ ages of 46.2 ± 0.9 Ma for 554, 55.8 ± 0.2 Ma for FC-1, 276.1 ± 1.3 for Trebilcock, 507.5 ± 0.7 Ma for Bananeira, and 559.9 ± 3.1 Ma for Manangotry. These ages are accurate to within 1.3, 0.2, 1.5, 0.3, and 0.9% of the reference values, respectively; we conservatively adopt a minimum uncertainty of 2% for all dates reported herein. Date uncertainties reported in this paper are in-run uncertainties, unless enclosed in square brackets—e.g., ±[8]—in which case they incorporate the long-term uncertainty of 2%. Xenotime grains in samples K1726G2 and M8713A2 were analyzed with the same protocol and returned identical ages for both phosphate minerals, implying that matrix effects for LREE and HREE phosphates are similar within uncertainty.

4. Results

Data were obtained from the western allochthons, eastern allochthons, WGC and metasediments overlying the WGC. The large size of this campaign-style dataset means that each sample cannot be discussed individually in the text. Hence, we summarize the data in Table 1 and give examples in Figs. 5–8 to summarize the complete dataset shown in Supplementary Fig. 1 and Supplementary Table 1.

All of the samples are amphibolite-facies rocks with biotite, plagioclase and quartz; many contain garnet, muscovite, kyanite, or sillimanite (Table 1). Staurolite, margarite, hornblende and xenotime are present in a few samples. Most have typical amphibolite-facies textures wherein the sheet silicates and elongate minerals are oriented, plagioclase and quartz are xenoblastic, and biotite, garnet, muscovite, kyanite, sillimanite, staurolite, and hornblende are hypidioblastic to idioblastic (Fig. 4A). Exceptions are noted in the text and in Supplementary Table 1.

4.1. Western allochthons monazite

Five samples were studied from the allochthons west of the WGR—specifically from the Hyllestad Complex in the Solund area (Fig. 1; "W.A." samples in Table 1). This area is of particular interest because it preserves aluminous high-pressure schists that might have formed coevally with the 425–400 Ma eclogite of the WGR [Chauvet et al.,

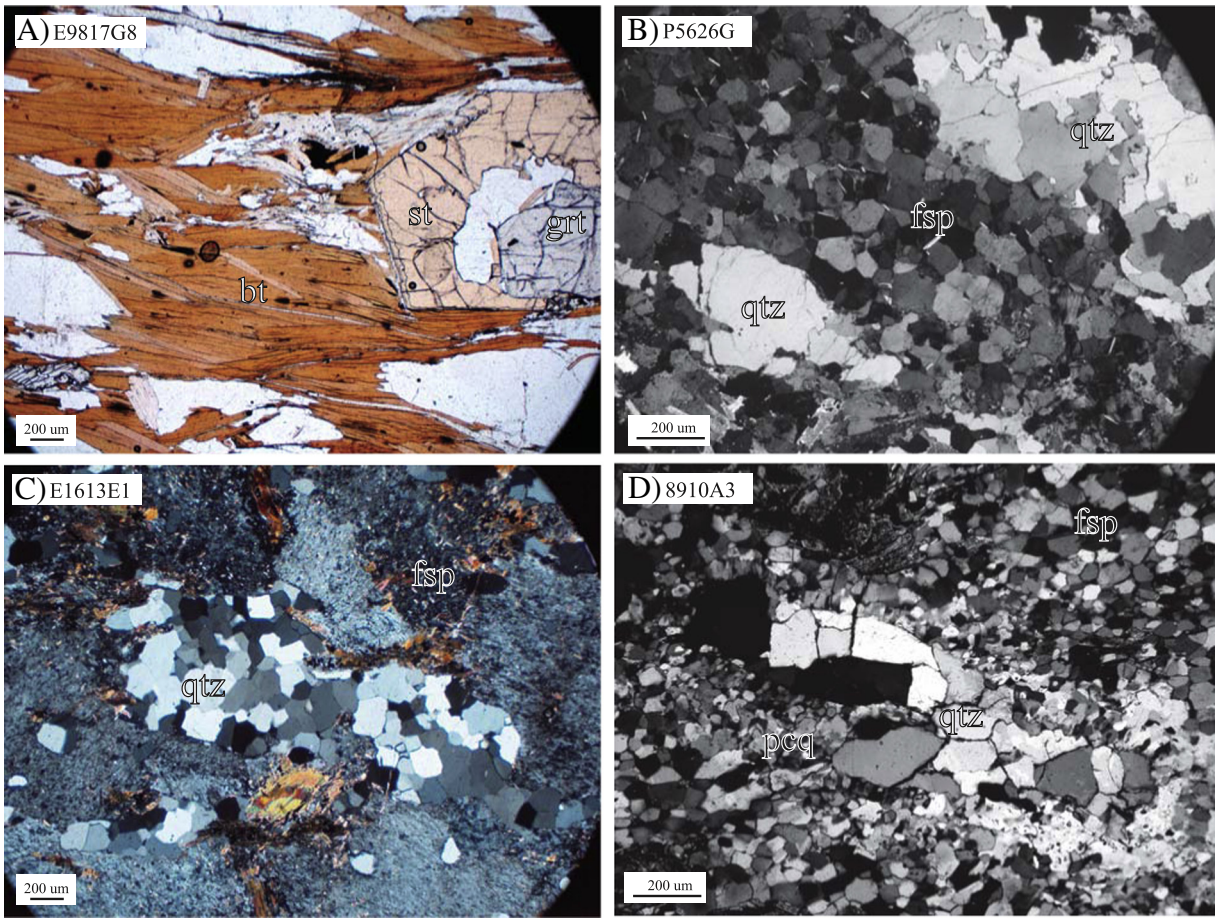

Fig. 4. Photomicrographs of rock microstructures. A) Amphibolite-facies minerals and microstructure typical of most of the samples in this study. B) Polygonized plagioclase indicating high-temperature deformation. C) Coesite pseudomorphs indicating recrystallization at high pressure. D) Polycrystalline quartz aggregates (pcq), suggestive of formation as coesite pseudomorphs.

1992; Hacker et al., 2003; Labrousse et al., 2004]. All the samples studied are metapelites strongly affected by sillimanite-stable deformation, lower amphibolite-facies deformation, and then chlorite-stable greenschist-facies brittle–ductile deformation. Monazite occurs as inclusions in garnet and as matrix grains; some grains are unusually large, reaching 200 μm. There are two types of samples: 1) The most-aluminous rocks are all from the same outcrop and have peak mineral assemblages of garnet + kyanite + muscovite + paragonite ± staurolite ± chloritoid that equilibrated at 600 °C and 1.5 GPa [Chauvet et al., 1992; Hacker et al., 2003; Labrousse et al., 2004]; this HP assemblage is overprinted principally by sillimanite. These samples gave monazite ages of 432 ± [8] Ma, 424 ± [8] Ma and 421 ± [8] Ma (Table 1, Fig. 3; Supplementary Table 1). 2) Two less-aluminous rocks that contain kyanite + garnet + muscovite + biotite ± staurolite equilibrated at 600 °C and 1.2 GPa. These samples yielded ages of 457 ± [9] Ma and 454 ± [9] Ma.

4.2. Eastern allochthons monazite

The largest allochthon outcrops are east of the WGR toward the foreland (Fig. 1; "E.A." samples in Table 1) in units that have been mapped and described as parts of the Gula, Seve, Essandsjø–Øyfjell, Surna, Osen–Roå, and Blåhø Nappes [e.g., Rickard, 1985; Kollung, 1990; Bjerkgård and Bjørlykke, 1994]. These rocks include metasandstone, calcareous phyllite, migmatitic gneiss, and pelite. All were intruded by a 438–430 Ma trondhjemite–diorite–gabbro suite [Olesen et al., 1973; Nilsen, 1978; Size, 1979; Pannemans and Roberts, 2000]. The igneous suite was preceded by an early regional metamorphism, and followed by a late regional metamorphism [Hacker and Gans, 2005]. Metamorphic conditions of ~600–750 °C and ~0.9–1.3 GPa are inferred for the regional metamorphism on the basis of mineral compositions and assemblages (Fig. 2) [Hacker and Gans, 2005].

Seven samples of the eastern allochthons were studied. All are typical amphibolite-facies, metapelitic schists and gneisses with low-variance assemblages of garnet–biotite–muscovite ± staurolite and kyanite–staurolite–garnet–biotite ± muscovite. Monazite occurs as inclusions in garnet and as matrix grains; most are relatively small at 10–20 μm. Most of the samples have monazite U–Pb spot dates that form single-age populations between 430 ± [9] Ma and 405 ± [8] Ma. Two samples yielded a range of spot dates, and two of those spot dates are as old as ~450 Ma (Table 1, Fig. 3; Supplementary Table 1).

4.3. Metasedimentary rocks atop the WGC

Thirty-two samples were analyzed from the metasedimentary rocks atop the WGC. Specific targets included metasedimentary units with and without eclogite inclusions; effort was made to study samples over a broad geographic area and to study samples with a well-constrained PT evolution. The samples are all composed of amphibolite-facies minerals, and most have textures typical of amphibolite-facies gneisses: a schistose to gneissic fabric defined by compositional banding and oriented platy or tabular minerals, feldspar porphyroclasts with recrystallized tails or feldspar completely recrystallized to fine grains, quartz with regime-II or regime-III microstructures [Hirth and Tullis, 1992], no localized deformation (e.g., no shear bands), no granulite-facies minerals, and no greenschist-facies minerals (Fig. 4A; thin section

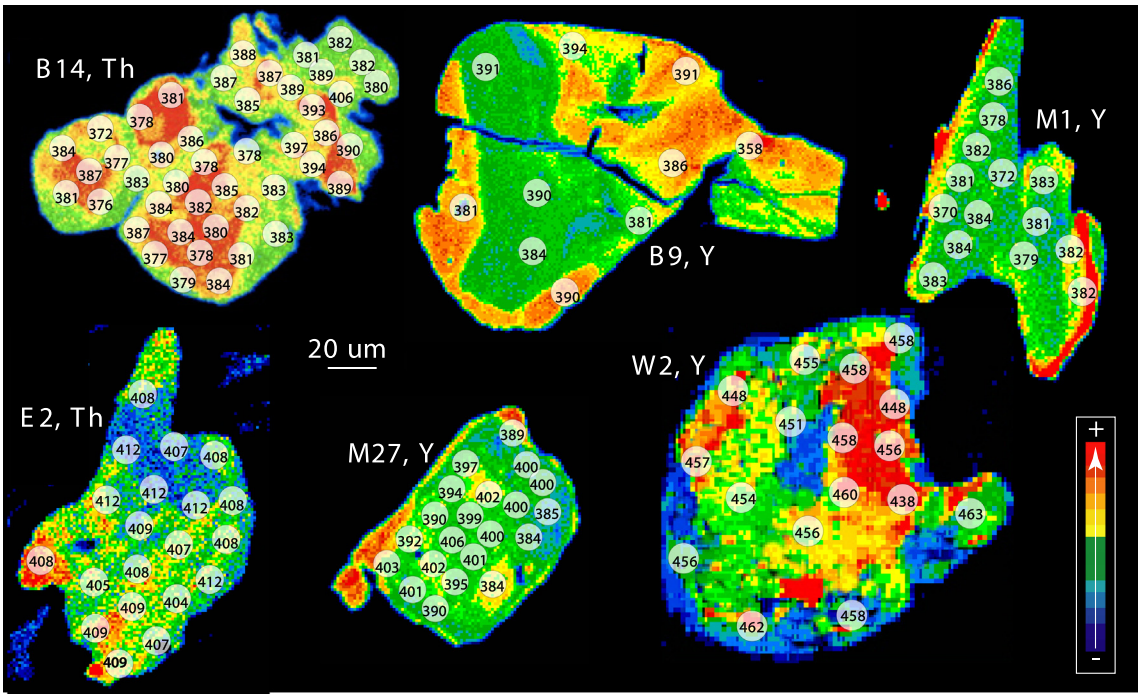

Fig. 5. Examples of Caledonian monazite with single date populations. Monazite Y or Th composition maps determined by X-ray counts; each grain scaled separately to highlight zoning (red shows high counts, blue low). Laser spots show $^{206}Pb/^{238}U$ dates. (For interpretation of the references to color in this figure legend, the reader is referred to the web version of this article.)

descriptions in Supplementary Fig. 1). The metapelites have a range of mineral assemblages whose low-variance members are sillimanite–garnet–biotite, kyanite–garnet–staurolite–biotite, and kyanite–garnet–biotite. In many samples, sillimanite postdates kyanite, or is unoriented or undeformed—and therefore late. A few samples have lower amphibolite-facies shear bands, a few are mylonitic, and one is an ultramylonite.

Most of the samples yielded Caledonian dates that form a single population (Fig. 5; 'single' in Table 1; Supplementary Fig. 1); the monazite ages from these samples range from 399 ± [8] Ma to 382 ± [8] Ma. Three samples yielded Caledonian monazite dates from 430 ± [9] Ma to 388 ± [8] Ma that do not form a single population ('multi' in Table 1); they are similar to the 'multi' samples discussed in detail below (Section 4.4.2).

4.4. Western gneiss complex

Twenty-three samples were analyzed from monazite-bearing rocks of the WGC. Specific targets included rocks with relict (U)HP minerals, inferred Caledonian igneous rocks, and inferred Precambrian igneous rocks, WGC basement. Geographic coverage was also considered.

The samples are all composed of amphibolite-facies minerals, and most have textures typical of amphibolite-facies gneisses (see thin section descriptions in Supplementary Fig. 1). Most of the monazites are 20–50 μm and nearly all are matrix grains along biotite or plagioclase grain boundaries; a few are sequestered in garnet. Whether individual grains are igneous, metamorphic or detrital may be difficult to assess, but some have patchy zoning suggestive of a metamorphic origin (e.g., B9 in Fig. 5, B2 in Fig. 6, and B12 in Fig. 7), whereas others have distinct oscillatory zoning compatible with growth from melt (e.g., B18 in Supplementary Fig. 1).

4.4.1. Single-population, Caledonian monazite

Nine samples yielded Caledonian dates that form a single population from 402 ± [8] to 383 ± [8] Ma (Figs. 3 and 5; 'single' in Table 1). Monazite is a matrix phase sited along biotite and/or feldspar grain boundaries; none is included in garnet. All but two of these samples have fine-grained, biotite laths distributed in feldspar + quartz aggregates suggestive of melt infiltration [Cesare, 2008].

4.4.2. Multi-population, Caledonian monazite

Another ten samples from the WGC yielded Caledonian monazite dates from 433 ± [9] Ma to 380 ± [8] Ma that do not form a single population (Figs. 3 and 6; 'multi' in Table 1). These multiple populations are associated with three principal texture types:

1) Different monazite grains, each with a distinct date population. As an example, Fig. 6a shows a single sample (B6) with monazite grains with different REE signatures and dates ranging from 421 to 387 Ma. These data suggest monazite (re)crystallization[2] at the times recorded by the discrete grain ages. Differences in grain composition presumably reflect differences in the local grain-scale chemical environment, the composition of precursor monazite, or the composition of the minerals that broke down to form monazite. In sample B6, the increase in HREE from 421 Ma to 387 Ma is compatible with garnet breakdown during this age range, and with the presence of resorbed garnet.
2) Individual monazite grains with cores and rims of different ages and compositions, separated by a sharp boundary (Fig. 6b–c). This texture is compatible with monazite (re)crystallization in two distinct pulses. The different trace-element compositions may reflect changes in mineral paragenesis—e.g., the high-Y rims in Fig. 6b–c are likely related to garnet breakdown between 403 Ma and 396 Ma in sample B21 (now with no garnet), and between 397 and 381 Ma in B1 (garnet is strongly resorbed).
3) Individual monazite grains with cores and rims of different age but nearly the same composition (Fig. 6d). In the example of Fig. 6d, the HREE abundances are similar for most analyses, but the Th

[2] We use (re)crystallization, for monazite where the texture is ambiguous, to indicate i) crystallization of a new grain or ii) recrystallization of an existing grain by any chemical or physical process.

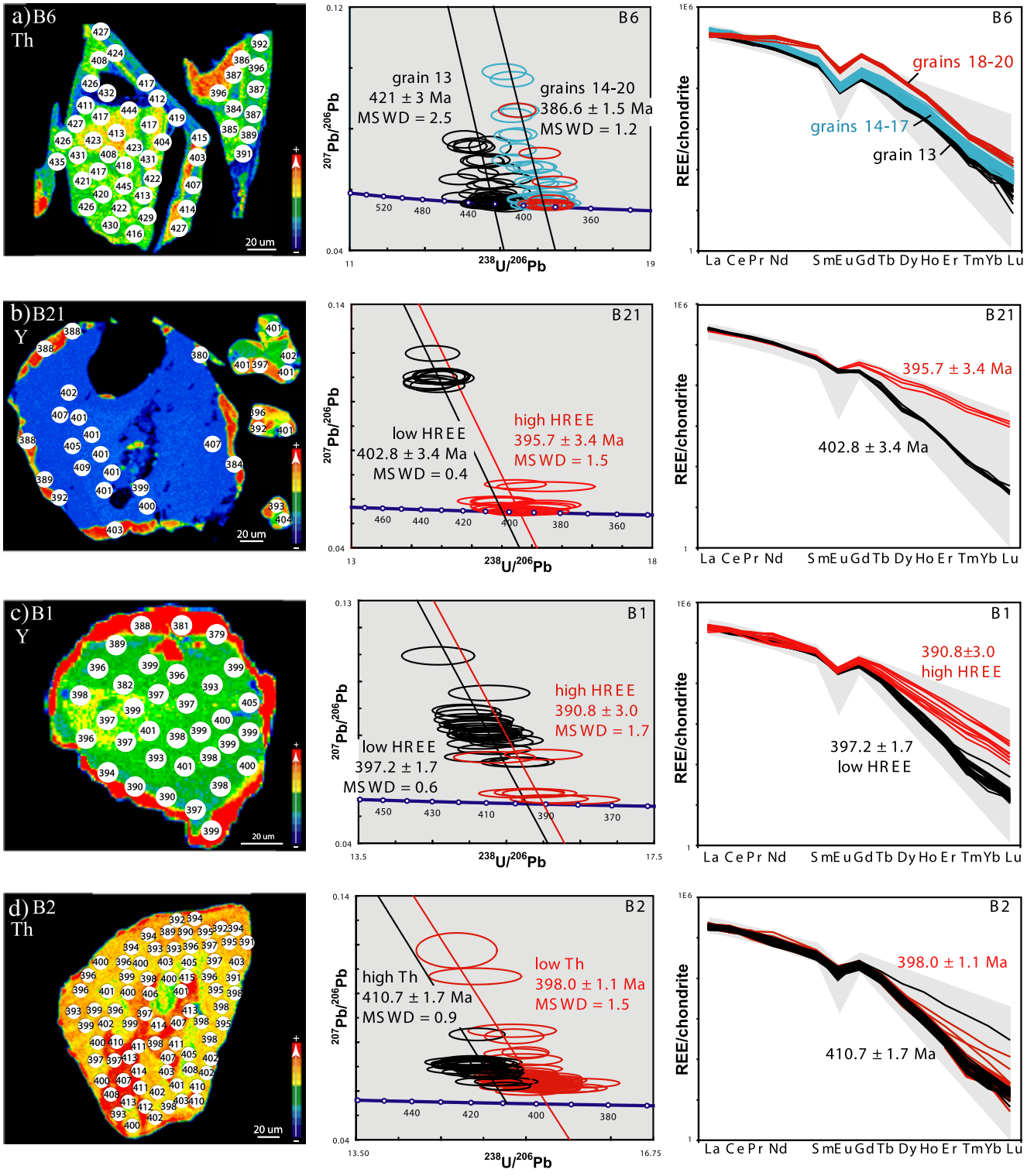

Fig. 6. Examples of monazite with multiple Caledonian dates. a) Different grains in B6 have similar Th zoning, but distinct ages and REE patterns. b) B21 grain core is homogenous in Y, has old ages, low HREE and high common Pb; patchy-zoned rims and smaller grains are younger, have elevated HREE and low common Pb. c) B1 grain core has old ages, low HREE and high common Pb; rims are younger, have elevated HREE and low common Pb. d) B2 grain core has old ages and higher Th; rims are younger and lower in Th [from Holder et al., 2015]. Left: Monazite composition maps determined by X-ray counts; red shows high counts, blue low. Laser spots show "207-corrected" $^{206}Pb/^{238}U$ dates. Middle: Isochrons anchored to Stacey–Kramers common $^{207}Pb/^{206}Pb$. Right: REE abundances color coded to middle column. Gray field shows entire range of monazite measured in this study. (For interpretation of the references to color in this figure legend, the reader is referred to the web version of this article.)

X-ray map shows a correlation between composition and date: the Th-rich portions are older and define an irregular red core in the X-ray image. The spot ages do not show a simple decrease from core to rim: the older spots are correlated with Th content and some are very near the grain rim. The lack of a simple core–rim age gradient indicates that the younger ages are not the result of simple volume diffusion. Indeed, the Th + age map in Fig. 6d is suggestive of fluid-assisted(?) recrystallization that progressed

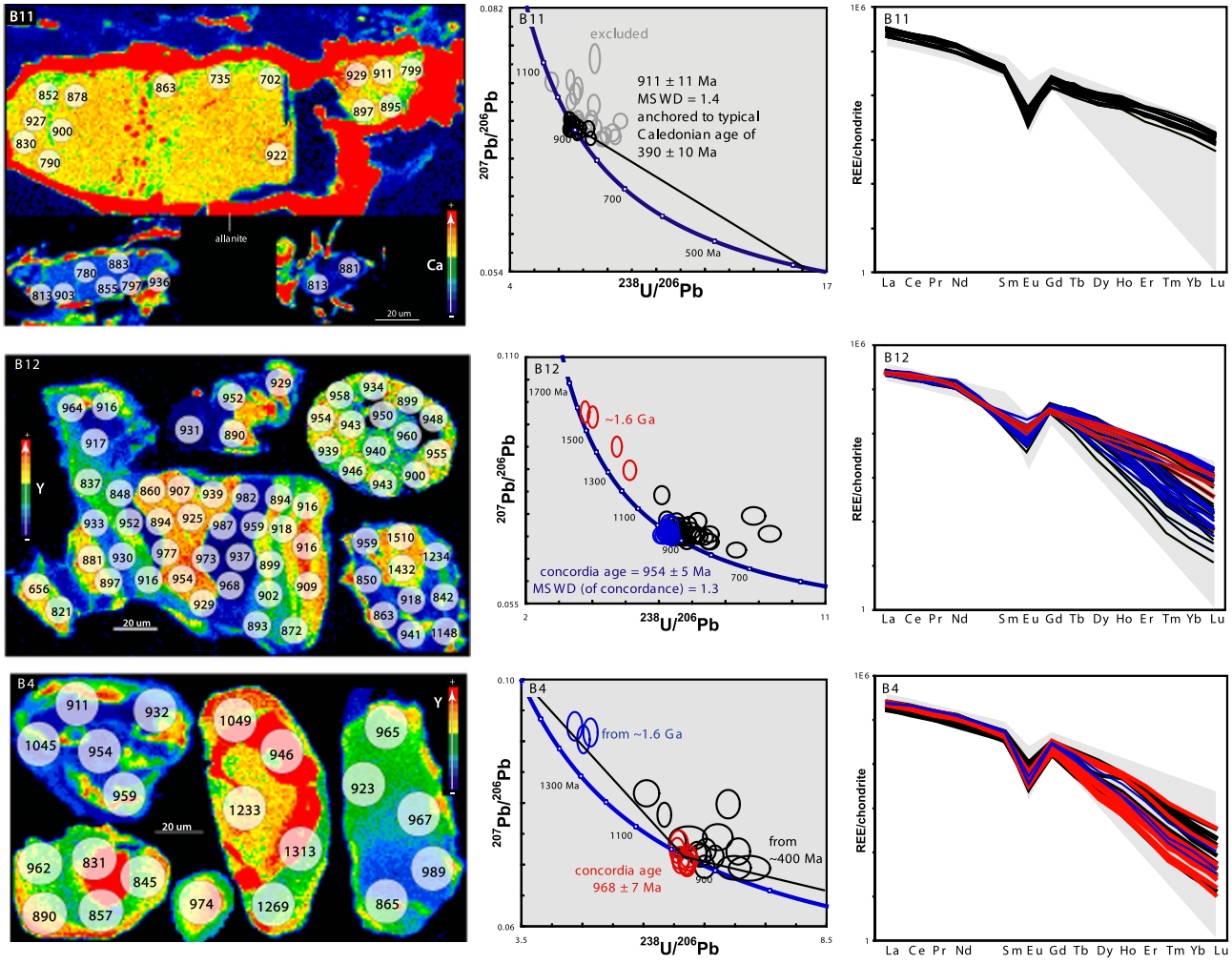

Fig. 7. Examples of Precambrian monazite. B11 gneiss with 911 Ma monazite partially altered to allanite; weak Caledonian resetting. Elevated HREE suggest that 911 Ma monazite grew before garnet coronae that are present along feldspar grain boundaries. B12 garnet-bearing gneiss. Transition from high to low HREE abundance at ~954 Ma presumably reflects first garnet growth. B4 garnet–sillimanite mylonite with chiefly 968 Ma monazite; weakness of Caledonian overprint suggests mylonitization is Precambrian. Left: Monazite composition maps determined by X-ray counts; red shows high counts, blue low. Laser spots show "207-corrected" $^{206}Pb/^{238}U$ dates. Middle: Isochrons anchored to Stacey–Kramers common $^{207}Pb/^{206}Pb$. Right: REE abundances color coded to middle column. Gray field shows entire range of monazite measured in this study. (For interpretation of the references to color in this figure legend, the reader is referred to the web version of this article.)

irregularly inward from the grain rim. Whether that recrystallization occurred over a protracted time interval—say from 405 to 390 Ma—or occurred at a specific time (e.g., 390 Ma) cannot be determined.

4.4.3. Precambrian monazite

Six samples have Precambrian monazite (1.6 Ga and ~950 Ma) with only a faint Caledonian overprint (Figs. 3 and 7; 'Pc' in Table 1; and Supplementary Fig. 1). All of these samples are adjacent to the Nordfjord UHP domain and are garnet-bearing gneisses characterized by high-temperature mineral assemblages (e.g., garnet–sillimanite) that likely developed at ≥800 °C [Spencer et al., 2013]. These samples are different from the other monazite-bearing amphibolite-facies samples in that they include polygonized plagioclase (Fsp in Fig. 4B), plagioclase with inclusions of <10-μm biotite and/or zoisite neoblasts, and undeformed allanite overgrowths on monazite (red in Fig. 7). The 1.6 Ga monazite present in four samples may be igneous, metamorphic, or detrital, whereas the 960–911(?) Ma monazite is likely metamorphic, based on similar metamorphic titanite dates from nearby rocks [Spencer et al., 2013]. The UHP tectonism and subsequent amphibolite-facies overprint caused minimal metamorphism of these rocks, limited to resetting of the K–Ar system in mica.

4.4.4. Precambrian–Caledonian monazite

Five samples have Precambrian monazite ages similar to those of the above samples, but also contain Caledonian monazite (Fig. 3; 'Pc/Caled' in Table 1; and Supplementary Fig. 1). The rocks have sillimanite–biotite, amphibolite-facies parageneses like most of the rocks in this study that contain Caledonian monazite. We interpret the Precambrian histories of these samples to be similar to the six with only Precambrian monazite (magmatic crystallization at 1.6 Ga with a 970–960 Ma granulite-facies metamorphism, or 970–960 Ma magmatism), but with a substantially stronger Caledonian overprint.

5. Discussion

This study examined monazite U–Pb dates in crystalline and metasedimentary rocks of the Scandinavian Caledonides that were subducted to pressures up to 3.6 GPa and temperatures up to 800 °C. The salient outcomes of this study are five. 1) Monazite in crystalline and metasedimentary rocks recorded quite different histories. 2) In spite of the high pressures and temperatures during subduction, some monazites retain pre-subduction dates. 3) Other monazites retain dates related to (U)HP subduction, but most recrystallized during the later exhumation event. 4) There is a spatial pattern to the monazite

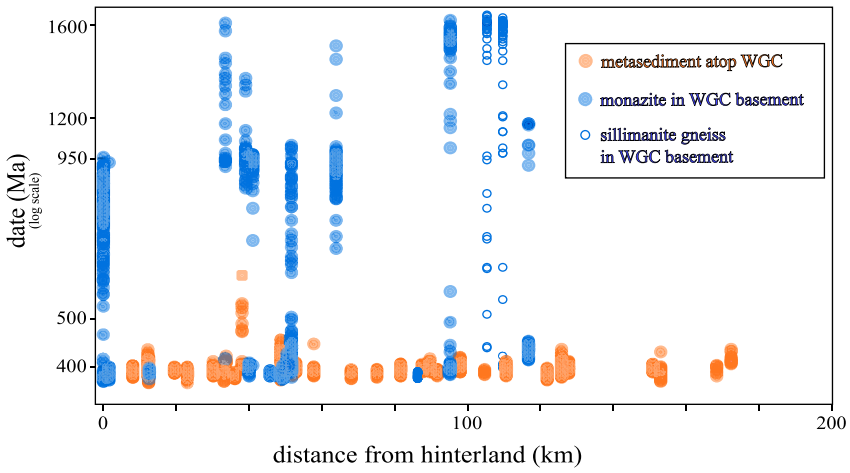

Fig. 8. Nearly all of the monazite from metasediment atop the WGC is Caledonian, whereas much of the monazite in the WGC basement is Precambrian. These data suggest that the metasediment is late Proterozoic to early Paleozoic in depositional age.

dates that is related to exhumation, with the youngest monazite in the west (Fig. 9). 5) Most monazite yielded concordant dates—as often assumed for monazite—but a few yielded U–Pb discordia.

5.1. Metasediment monazite is Caledonian; WGC monazite is Precambrian–Caledonian

As shown in Fig. 8, nearly all the monazite from metasedimentary rock atop the WGC is Caledonian; and—aside from one sample—all of the Precambrian monazite is within rocks from the WGC. The simplest interpretation is that the metasedimentary rocks dated in this study were deposited during the late Proterozoic to early Paleozoic and were not metamorphosed prior to the Caledonian. There are, however, Proterozoic (~0.95 Ga) monazites in metasedimentary rocks atop the WGC on Hisarøya (south of Fig. 1) [Røhr et al., 2004], indicating that the metasediments locally have depositional ages >0.95 Ga. If any of the dated metasedimentary rocks in this study were also deposited and metamorphosed during the Precambrian, they have been extensively recrystallized in the Caledonian—perhaps because of a different grain size, composition, melting temperature, or degree of deformation.

5.2. Why did some Precambrian monazite survive subduction?

Monazite in the WGC basement has both Precambrian and Caledonian ages. Six samples have Precambrian monazite (1.6 Ga and ~950 Ma) with only a faint Caledonian overprint. As noted above, all six are adjacent to the southernmost UHP domain, where Caledonian temperatures were lowest, ≤750 °C, and colder than the earlier, Precambrian metamorphism at ≥800 °C [Spencer et al., 2013]. These samples have polygonized plagioclase (Fig. 4B), a texture different than the rest of the samples in this study. Polygonized plagioclase is the result of high-temperature deformation at pressures where plagioclase is stable; the polygonization either i) predates the Caledonian subduction and the plagioclase was metastable during subduction, or ii) indicates strong, pervasive deformation after subduction. That the monazite coexisting with the polygonized plagioclase is Precambrian implies that the plagioclase was metastable during subduction.

Another five WGC samples with partially Caledonized Precambrian monazite are all from farther north than the six exclusively Precambrian samples, and reached higher Caledonian temperatures of ≥750 °C [Spencer et al., 2013]. Thus, a reasonable explanation for the persistence of Precambrian monazite in some WGC samples is that those samples were converted in the Precambrian to a relatively dry, granulite-facies metamorphic mineral assemblage that was resistant to resetting [Hacker, 1996], and the colder Caledonian metamorphism [Corfu et al., 2013] was unable to induce monazite recrystallization. The preservation of Precambrian monazite is yet another indication that that large portions of the WGC did not deform during subduction and exhumation [Krabbendam et al., 2000; Austrheim et al., 2003; Peterman et al., 2009; Hacker et al., 2010; Spencer et al., 2013; Kylander-Clark and Hacker, 2014].

5.3. Why do some monazite preserve 'UHP' dates?

Although we have established that most of the monazite from metasedimentary rocks is Caledonian, we can be even more specific: most of the monazite from metasedimentary rocks does not record the profound UHP metamorphism (i.e., ≥405 Ma), but is younger; only three metasedimentary samples [M4, M6, M28, Holder et al., 2015] of thirty-two have dates coeval with UHP metamorphism. Interestingly, these three samples are not different from the other twenty-nine in terms of mineralogy, grain size, deformation, monazite size, monazite texture, etc. The only *potentially* meaningful observation—and it is not a strong one—is that two of the three samples that retain syn-UHP dates are in a UHP domain. Why this should be so is unclear, unless the higher pressures were more conducive to monazite (re)crystallization.

A similar difference holds for monazite from the WGC. Of the twenty WGC samples with Caledonian monazite, only four (B2, B6, B24, B27) have syn-UHP dates; the rest do not. Among these samples, B2 contains unusual polycrystalline biotite clots, corundum + plagioclase, and polycrystalline-quartz coesite pseudomorphs (Fig. 4C,D [Lenze and Stöckhert, 2007]) suggesting that this rock was once a high-pressure gneiss that backreacted to low-P minerals during exhumation; the other three samples have typical amphibolite-facies mineralogies and textures. Again, the only potentially meaningful observation is that three of the four samples that retain syn-UHP dates are in UHP domains.

5.4. Spatial pattern of monazite dates

Ideally, we want to be able to associate each particular monazite date with the age of a specific geologic event or process. Aside from examples discussed above, however, it is difficult to equate metamorphic monazite recrystallization with a particular geologic event in most samples in this study. The fact that most of the samples are amphibolite-facies rocks with typical amphibolite-facies mineral assemblages and textures, and most of the monazite are matrix phases along grain boundaries, means that recrystallization could have been in response to deformation, fluid influx, melt crystallization, Ostwald ripening and/or changes in P or T. There are, however, two observations that may be relevant.

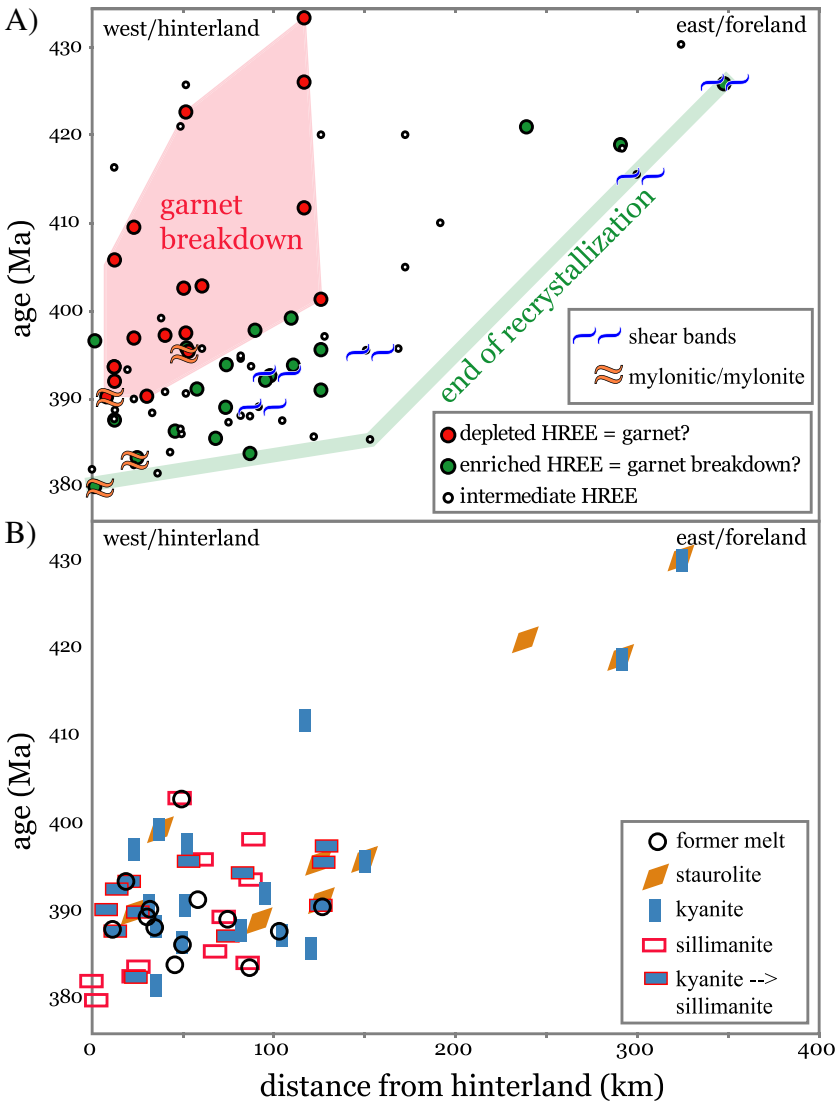

Fig. 9. A) Relationship between monazite U–Pb date, HREE abundance, deformation, and location (distance with respect to location of sample B18). Youngest monazite dates decrease westward, defining westward-sweeping end of recrystallization. The transition from monazite depleted in HREE to monazite enriched in HREE decreases in age westward, defining the westward progression of garnet breakdown. Samples with localized deformation tend to be among the youngest at all locations. B) There is no systematic relationship between monazite U–Pb date, rock mineralogy, and location. Only the youngest date in each sample is shown; western allochthons are not shown because their position prior to late, large-scale westward displacement is unknown.

1) The monazite dates are weakly correlated with distance from the foreland (colored symbols in Fig. 3). First, the dates of the youngest monazite decrease westward (Figs. 9 and 10), requiring that whatever geologic process terminated monazite recrystallization progressed westward. Similar patterns have been noted for U–Pb titanite [Spencer et al., 2013] and $^{40}Ar/^{39}Ar$ mica [Walsh et al., 2013] dates in the WGR, and ascribed to westward-propagating unroofing—meaning that the end of recrystallization could have been caused by the end of deformation, waning temperature, or decompression-induced melting. Second, Caledonian monazite with low HREE abundances tends to be older than monazite with high HREE abundances (Fig. 9), suggesting that the two groups of samples bracket the time of garnet breakdown. This transition becomes younger westward—~395 Ma in the east and ~385 Ma in the west—again compatible with westward-propagating unroofing. Third, samples with shear bands overprinting the typical amphibolite-facies fabric are among the youngest everywhere (Fig. 9), compatible with strain localization during unroofing. Fourth, all four mylonitic/mylonite samples are in the hinterland (Figs. 9A and 10), again indicating increasing strain localization during westward-propagating unroofing. (In spite of the fact that sillimanite postdates kyanite or is unoriented and/or undeformed—and therefore late—in most samples, Fig. 9B shows no systematic relationship between monazite age and mineral assemblage.) Fifth, the western and eastern allochthons have exclusively older Caledonian monazite (Fig. 3).
2) There is a slight increase in the uranium content of Caledonian monazite over time after ~410 Ma (Supplemental Fig. 1). Uranium is a H_2O-soluble element, *suggesting* the influx of U during exhumation-related hydration. The compositions of Caledonian leucosomes and pegmatites in the WGR also indicate fluid influx during the amphibolite-facies metamorphism [Ganzhorn et al., 2014]. Monazite is unusually susceptible to fluid-induced recrystallization [Budzyń et al., 2011], and some of the textures seen in Figs. 5–7 are compatible with inward propagation of a fluid-mediated reaction front.

Thus, the westward progression of the end of monazite recrystallization (Figs. 3, 9 and 10) most likely marks unroofing of the (U)HP WGR, given i) the correlation with similar gradients in U–Pb titanite dates and

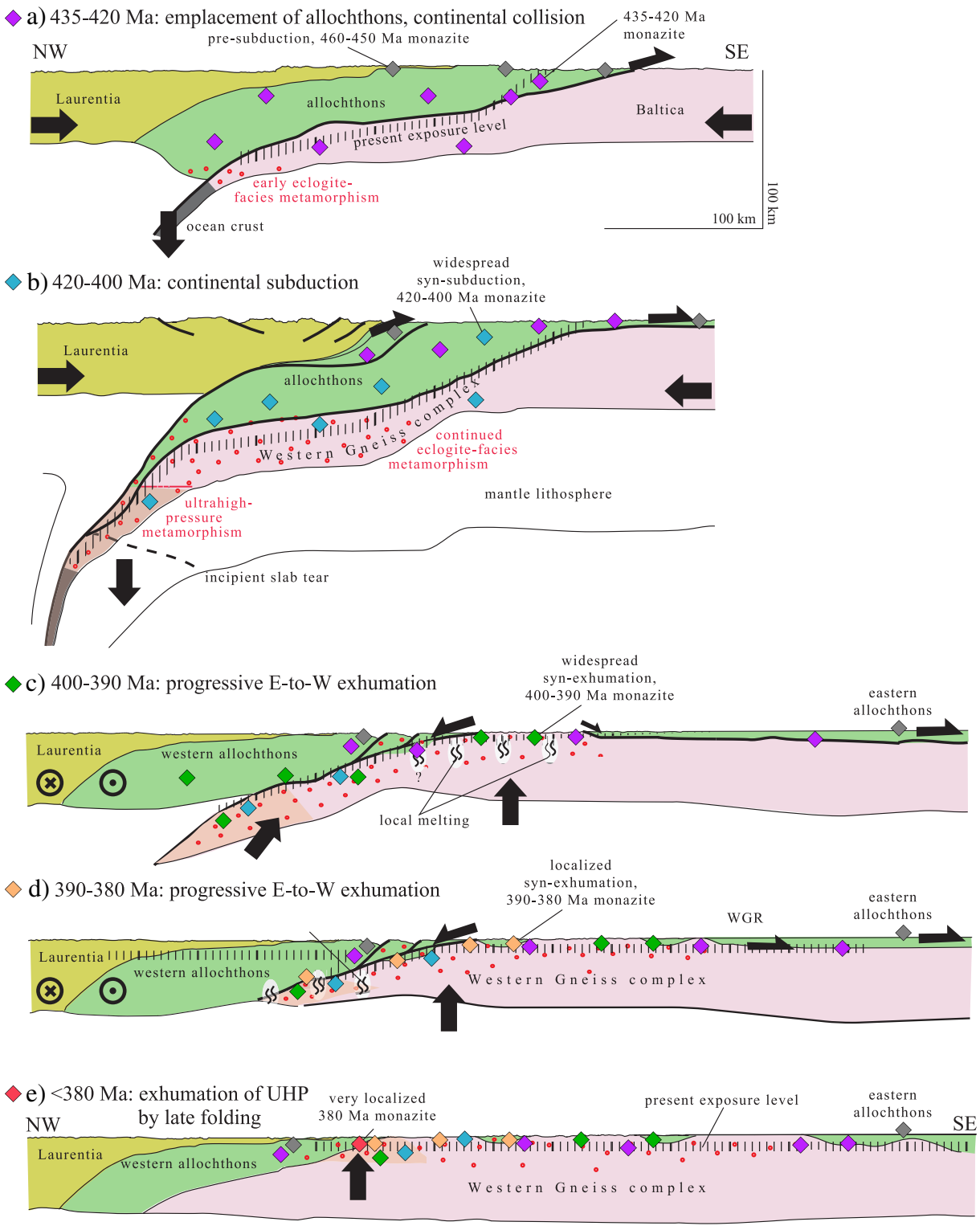

Fig. 10. Tectonic history of the Western Gneiss Region and surrounding area, focusing on monazite. Pre-subduction 460–450 Ma monazite are preserved at structurally high levels in allochthons (green) west and east of the Western Gneiss Region basement culmination (pink). 430–400 Ma monazite formed during subduction of allochthons and basement is preserved chiefly in allochthons, but locally in basement. Progressive E–W unroofing caused monazite recrystallization from 400 to 385 Ma across the basement and immediately overlying central allochthons. Compare with tectonic history inferred from U–Pb titanite dates, $^{40}Ar/^{39}Ar$ mica dates, and structural geology [Hacker et al., 2010; Spencer et al., 2013]. (For interpretation of the references to color in this figure legend, the reader is referred to the web version of this article.)

$^{40}Ar/^{39}Ar$ mica dates, ii) the correlation with garnet decomposition inferred from HREE abundances (Fig. 9), and iii) that the samples that show strain localization (i.e., are mylonitic or have shear bands) are among the youngest across the WGR. At the sample scale, whether monazite recrystallization was driven by deformation, fluid influx, melt crystallization or changes in P and T is resolved only in samples that are mylonitic or have textures suggestive of fluid-induced recrystallization (Figs. 5–7).

6. Conclusions

U–Pb dates and trace-element concentrations were measured from sixty-nine monazite-bearing crystalline basement and metasedimentary rocks from the (U)HP Western Gneiss Region. 1) Nearly all of the monazite from the metasedimentary rocks is Caledonian, whereas much of the crystalline basement contains Precambrian monazite; this is potentially explained by deposition of the sediment during the late Proterozoic to early Paleozoic after Precambrian metamorphism. 2) Half of the basement samples—particularly those in the south where temperatures reached during subduction were lower—contain Precambrian monazite that was incompletely reset during subduction and exhumation; this is likely due to sluggish reaction kinetics in rocks that were rendered relatively dry and coarse grained by a hot Precambrian metamorphism. 3) A few monazite dates from metasedimentary rocks atop the Western Gneiss Complex record recrystallization during subduction; many are located in UHP domains. 4) Caledonian monazite dates generally young westward, compatible with the westward progression of unroofing of the WGR inferred from other datasets.

Acknowledgments

This study was funded by US NSF grants EAR-1219942, EAR-0911485, and EAR-0923552, and UCSB. Torgeir B. Andersen was funded by Norwegian Research Council Centre of Excellence grants (223272 to CEED and PGP). The electron imaging facility is operated by Gareth Seward; that facility and the LASS facility are supported by Howard Berg. The samples analyzed here were collected during fieldwork with Steven Arauza, Adam Ginsburg, Stacia Gordon, Scott Johnston, and Katherine Spencer. This manuscript was reviewed by John Cottle, Josh Garber, and Forrest Horton.

Appendix A. Supplementary data

Supplementary data to this article can be found online at http://dx.doi.org/10.1016/j.chemgeo.2015.05.008.

References

Aleinikoff, J.N., 2006. Deciphering igneous and metamorphic events in high grade rocks of the Wilmington Complex, Delaware: morphology, CL and BSE zoning, and SHRIMP U–Pb geochronology of zircon and monazite. Geol. Soc. Am. Bull. 118, 39–64.

Andersen, T.B., Skjerlie, K.P., Furnes, H., 1990. The Sunnfjord Melange, evidence of Silurian ophiolite accretion in the West Norwegian Caledonides. J. Geol. Soc. Lond. 147, 59–68.

Andersen, T.B., Jamtveit, B., Dewey, J.F., Swensson, E., 1991. Subduction and eduction of continental crust: major mechanism during continent–continent collision and orogenic extensional collapse, a model based on the south Caledonides. Terra Nova 3, 303–310.

Andersen, T.B., Corfu, F., Labrousse, L., Osmundsen, P.T., 2012. Evidence for hyperextension along the pre-Caledonian margin of Baltica. 169, 601–612.

Austrheim, H., Corfu, F., Bryhni, I., Andersen, T.B., 2003. The Proterozoic Hustad igneous complex: a low strain enclave with a key to the history of the Western Gneiss Region of Norway. Precambrian Res. 120, 149–175.

Beckman, V., Möller, C., Söderlund, U., Corfu, F., Pallon, J., Chamberlain, K.R., 2014. Metamorphic zircon formation at the transition from gabbro to eclogite in Trollheimen–Surnadalen, Norwegian Caledonides. Geol. Soc. Lond., Spec. Publ. 390, 403–424.

Bjerkgård, T., Bjørlykke, A., 1994. Geology of the Folldal area, southern Trondheim region Caledonides, Norway. Norges Geol. Unders. Bull. 426, 53–75.

Bryhni, I., 1989. Status of the supracrustal rocks in the Western Gneiss Region, S. Norway. In: Gayer, R.A. (Ed.), The Caledonide Geology of Scandinavia. Graham and Trotman, London, pp. 221–228.

Budzyń, B., Harlov, D.E., Williams, M.L., Jercinovic, M.J., 2011. Experimental determination of stability relations between monazite, fluorapatite, allanite, and REE-epidote as a function of pressure, temperature, and fluid composition. Am. Mineral. 96, 1547–1567.

Cesare, B., 2008. Crustal melting: working with enclaves. In: Sawyer, E.W., Brown, M. (Eds.), Working With Migmatites. Mineralogical Association of Canada Short Course Series vol. 38, pp. 37–55.

Chauvet, A., Kienast, J.R., Pinardon, J.L., Brunel, M., 1992. Petrological constraints and PT path of Devonian collapse tectonics within the Scandian mountain belt (Western Gneiss Region, Norway). J. Geol. Soc. Lond. 149, 383–400.

Corfu, F., Andersen, T.B., 2002. U–Pb ages of the Dalsfjord Complex, SW Norway, and their bearing on the correlation of allochthonous crystalline segments of the Scandinavian Caledonides. Int. J. Earth Sci. 91, 955–963.

Corfu, F., Torsvik, T.H., Andersen, T.B., Ashwal, L.D., Ramsay, D.M., Roberts, R.J., 2006. Early Silurian mafic–ultramafic and granitic plutonism in contemporaneous flysch, Magerøy, northern Norway: U–Pb ages and regional significance. J. Geol. Soc. 163, 291–301.

Corfu, F., Austrheim, H., Ganzhorn, A.C., 2013. Localized granulite and eclogite facies metamorphism at Flatraket and Krakeneset, Western Gneiss Region: U–Pb data and tectonic implications. In: Corfu, F., Gasser, D., Chew, D.M. (Eds.), New Perspectives on the Caledonides of Scandinavia and Related Areas. Geological Society, London, Special Publications. vol. 390. The Geological Society of London. http://dx.doi.org/10.1144/SP390.22 (pp.).

Cuthbert, S.J., Carswell, D.A., Krogh-Ravna, E.J., Wain, A., 2000. Eclogites and eclogites in the Western Gneiss Region, Norwegian Caledonides. Lithos 52, 165–195.

Fauconnier, J., Labrousse, L., Andersen, T.B., Beyssac, O., Duprat-Oualid, S., Yamato, P., 2014. Thermal structure of a major crustal shear zone, the basal thrust in the Scandinavian Caledonides. Earth Planet. Sci. Lett. 385, 162–171.

Finger, 1998. Replacement of primary monazite by apatite–allanite–epidote coronas in an amphibolite facies granite gneiss from the eastern Alps. Am. Mineral. 83, 248–258.

Finger, F., Krenn, E., 2007. Three metamorphic monazite generations in a high-pressure rock from the Bohemian Massif and the potentially important role of apatite in stimulating polyphase monazite growth along a PT loop. Lithos 95, 103–115.

Franz, G., Andrehs, G., Rhede, D., Ayora, C., 1996. Crystal chemistry of monazite and xenotime from Saxothuringian–Moldanubian metapelites, NE Bavaria, Germany. Eur. J. Mineral. 8, 1097–1118.

Ganzhorn, A.C., Labrousse, L., Proteau, G., Leroy, C., Vrijmoed, J.C., Andersen, T.B., Arbaret, L., 2014. Structural, petrological and chemical analysis of syn-kinematic migmatites: insights from the Western Gneiss Region, Norway. J. Metamorph. Geol. 32, 647–673.

Gee, D.G., 1980. Basement–cover relationships in the central Scandinavian Caledonides. Geol. Fören. Stockh. Förh. 102, 455–474.

Glodny, J., Kühn, A., Austrheim, H., 2008. Diffusion versus recrystallization processes in Rb–Sr geochronology: isotopic relics in eclogite facies rocks, Western Gneiss Region, Norway. Geochim. Cosmochim. Acta 72, 506–525.

Gordon, S.M., Whitney, D.L., Teyssier, C., Fossen, H., 2013. U–Pb dates and trace-element geochemistry of zircon from migmatite, Western Gneiss Region, Norway: significance for history of partial melting in continental subduction. Lithos 170–171, 35–53.

Gratz, R., Heinrich, W., 1997. Monazite–xenotime thermometry: experimental calibration of the miscibility gap in the binary system CePO4–YPO4. Am. Mineral. 82, 772–780.

Hacker, B.R., 1996. Eclogite formation and the rheology, buoyancy, seismicity, and H_2O content of oceanic crust. In: Bebout, G.E., Scholl, D., Kirby, S.H., Platt, J.P. (Eds.), Dynamics of Subduction. vol. 96. American Geophysical Union, Washington, D.C., pp. 337–346.

Hacker, B.R., 2006. Pressures and temperatures of ultrahigh-pressure metamorphism: implications for UHP tectonics and H_2O in subducting slabs. Int. Geol. Rev. 48, 1053–1066.

Hacker, B.R., Gans, P.B., 2005. Creation of ultrahigh-pressure terranes: the Trøndelag–Jämtland region of the Scandinavian Caledonides. Geol. Soc. Am. Bull. 117, 117–134.

Hacker, B.R., Andersen, T.B., Root, D.B., Mehl, L., Mattinson, J.M., Wooden, J.L., 2003. Exhumation of high-pressure rocks beneath the Solund Basin, Western Gneiss Region of Norway. J. Metamorph. Geol. 21, 613–629.

Hacker, B.R., Andersen, T.B., Johnston, S., Kylander-Clark, A.R.C., Peterman, E., Walsh, E.O., Young, D., 2010. High-temperature deformation during continental-margin subduction & exhumation: the ultrahigh-pressure Western Gneiss Region of Norway. Tectonophysics 480, 149–171.

Harrison, T.M., McKeegan, K.D., Le Fort, P., 1995. Detection of inherited monazite in the Manaslu leucogranite by $^{208}Pb/^{232}Th$ ion microprobe dating. Earth Planet. Sci. Lett. 133, 271–282.

Harrison, T.M., G. M, M.K. D, Coath, C.D., Lovera, O.M., Le Fort, P., 1999. Origin and episodic emplacement of the Manaslu intrusive complex, central Himalaya. J. Petrol. 40, 3–19.

Hernes, I., 1956. The Surnadal syncline, central Norway. Nor. Geol. Tidsskr. 36, 25–36.

Hirth, G., Tullis, J., 1992. Dislocation creep regimes in quartz aggregates. J. Struct. Geol. 14, 145–159.

Holder, R., Hacker, B., Kylander-Clark, A., Cottle, J., 2015. Monazite Trace-element and Isotopic Signatures of (Ultra)high-pressure Metamorphism: Examples From the Western Gneiss Region, Norway. Chemical Geology. http://dx.doi.org/10.1016/j.chemgeo.2015.04.021.

Horstwood, M.S.A., Foster, G.L., Parrish, R.R., Noble, S.R., Nowell, G.M., 2003. Common-Pb corrected in situ U–Pb accessory mineral geochronology by LA-MC-ICP-MS. J. Anal. At. Spectrom. 18, 837–846.

Hoskin, P.W.O., Schaltegger, U., 2003. The composition of zircon and igneous and metamorphic petrogenesis. Rev. Mineral. Geochem. 53, 27–62.

Johnston, S., Hacker, B.R., Andersen, T.B., 2007a. Exhuming Norwegian ultrahigh-pressure rocks: overprinting extensional structures and the role of the Nordfjord–Sogn Detachment Zone. Tectonics 26, TC5001. http://dx.doi.org/10.1029/2005TC001933.

Johnston, S., Hacker, B.R., Ducea, M.N., 2007b. Exhumation of ultrahigh-pressure rocks beneath the Hornelen segment of the Nordfjord–Sogn Detachment Zone, western Norway. Geol. Soc. Am. Bull. 119, 1232–1248.

Kingsbury, J.A., Miller, C.F., Wooden, J.L., Harrison, T.M., 1993. Monazite paragenesis and U–Pb systematics in rocks of the eastern Mojave Desert, California, USA: implications for thermochronometry. Chem. Geol. 110, 147–167.

Kelsey, D.E., 2008. On ultrahigh-temperature crustal metamorphism. Gondwana Res. 13, 1–29.

Kollung, S., 1990. The Surna, Rinna, and Orkla Nappes of the Surnadal–Orkdal district, southwestern Trondheim Region. Nor. Geol. Unders. 418, 9–17.

Kosler, J., Tubrett, M.N., Sylvester, P.J., 2001. Application of laser ablation ICP-MS to U–Th–Pb dating of monazite. Geostand. Newslett. 25, 375–386.

Krabbendam, M., Wain, A., Andersen, T.B., 2000. Pre-Caledonian granulite and gabbro enclaves in the Western Gneiss Region, Norway: indications of incomplete transition at high pressure. Geol. Mag. 137, 235–255.

Krogh, E.J., 1977. Evidence of Precambrian continent–continent collision in Western Norway. Nature 267, 17–19.
Krogh, T., Kamo, S.L., Robinson, P., Terry, M.P., Kwok, Y., 2011. U–Pb zircon geochronology of eclogites from the Scandian Orogen, northern Western Gneiss Region, Norway: 14–20 million years between eclogite crystallization and return to amphibolite-facies conditions. Can. J. Earth Sci. 48, 441–472.
Kylander-Clark, A., Hacker, B.R., 2014. Age and significance of felsic dikes from the UHP Western Gneiss Region. Tectonics 33. http://dx.doi.org/10.1002/2014TC003582.
Kylander-Clark, A.R.C., Hacker, B.R., Mattinson, J.M., 2008. Slow exhumation of UHP terranes: titanite and rutile ages of the Western Gneiss Region, Norway. Earth Planet. Sci. Lett. 272, 531–540.
Kylander-Clark, A.R.C., Hacker, B.R., Johnson, C.M., Beard, B.L., Mahlen, N.J., 2009. Slow subduction of a thick ultrahigh-pressure terrane. Tectonics. http://dx.doi.org/10.1029/2007TC002251.
Kylander-Clark, A.R.C., Hacker, B.R., Cottle, J.M., 2013. Laser-ablation split-stream ICP petrochronology. Chem. Geol. http://dx.doi.org/10.1016/j.chemgeo.2013.02.019.
Labrousse, L., Jolivet, L., Andersen, T.B., Agard, P., Maluski, H., Schärer, U., 2004. Pressure–temperature–time–deformation history of the exhumation of ultra-high pressure rocks in the Western Gneiss region, Norway. In: Whitney, D.L., Teyssier, C., Siddoway, C.S. (Eds.), Gneiss Domes in Orogeny, Geological Society of America Special Paper. vol. 380. Geological Society of America, pp. 155–185.
Lenze, A., Stöckhert, B., 2007. Microfabrics of UHP metamorphic granites in the Dora Maira Massif, western Alps — no evidence of deformation at great depth. J. Metamorph. Geol. 25, 461–475.
Ludwig, K.R., 2003. Isoplot 3.00. A Geochronological Toolkit for Microsoft Excel. Berkeley Geochronology Center Special Publication 4.
Nilsen, O., 1978. Caledonian sulphide deposits and minor iron-formations from the southern Trondheim region, Norway. Norges Geol. Unders. Bull. 340, 35–85.
Olesen, N.Ø., Hansen, E.S., Kristensen, L.H., Thyrsted, T., 1973. Preliminary account on the geology of the Selbu–Tydal area, the Trondheim region, central Norwegian Caledonides. Leidse. Geol. Meded. 49, 259–276.
Palin, R.M., Searle, M.P., Waters, D.J., Parrish, R.R., Roberts, N.M.W., Horstwood, M.S.A., Yeh, M.-W., Chung, S.-L., Anh, T.T., 2013. A geochronological and petrological study of anatectic paragneiss and associated granite dykes from the Day Nui Con Voi metamorphic core complex, North Vietnam: constraints on the timing of metamorphism within the Red River shear zone. J. Metamorph. Geol. 31, 359–387.
Pannemans, B., Roberts, D., 2000. Geochemistry and petrogenesis of trondhjeimites and granodiorite from Gauldalen, central Norwegian Caledonides. Norges Geol. Unders. Bull. 437, 43–56.
Paton, C., Hellstrom, J.C., Paul, B., Woodhead, J.D., Hergt, J.M., 2011. Iolite: freeware for the visualisation and processing of mass spectrometer data. J. Anal. At. Spectrom. http://dx.doi.org/10.1039/clja10172b.
Peterman, E.M., Hacker, B.R., Baxter, E.F., 2009. Phase transformations of continental crust during subduction and exhumation: Western Gneiss Region, Norway. Eur. J. Mineral. 21, 1097–1118.
Peterman, E.M., Mattinson, J.M., Hacker, B.R., 2012. Multi-step TIMS and CA-TIMS to monazite U–Pb geochronology. Chem. Geol. 312–313, 58–73.
Pyle, J.M., Spear, F.S., Rudnick, R.L., McDonough, W.F., 2001. Monazite–xenotime and monazite–garnet equilibrium in a prograde pelite sequence. J. Petrol. 42, 2083–2117.
Ravna, E.J.K., Terry, M.P., 2004. Geothermobarometry of phengite–kyanite–quartz/coesite eclogites. J. Metamorph. Geol. 22, 579–592.
Rickard, M.J., 1985. The Surnadal synform and basement gneisses in the Surnadal–Sunndal district of Norway. In: Gee, D.G., Sturt, B.A. (Eds.), The Caledonide Orogen — Scandinavia and Related Areas. vol. 1. John Wiley and Sons, Chichester, pp. 485–497.
Roberts, D., Gee, D.G., 1985. An introduction to the structure of the Scandinavian Caledonides. In: Gee, D.G., Sturt, B.A. (Eds.), The Caledonide Orogen—Scandinavia and Related Areas. vol. Part 1. John Wiley and Sons, Chichester, pp. 55–68.
Robinson, P., 1995. Extension of Trollheimen tectono-stratigraphic sequence in deep synclines near Molde and Brattvåg, Western Gneiss Region, southern Norway. Nor. Geol. Tidsskr. 75, 181–198.
Roffeis, C., Corfu, F., 2014. Caledonian nappes of southern Norway and their correlation with Sveconorwegian basement domains. Geol. Soc. Lond., Spec. Publ. 390, 193–221.
Røhr, T.S., Corfu, F., Austrheim, H., Andersen, T.B., 2004. Sveconorwegian U–Pb zircon and monazite ages of granulite-facies rocks, Hisarøya Gulen, Western Gneiss Region, Norway. Nor. J. Geol. 84, 251–256.
Root, D.B., Hacker, B.R., Gans, P., Eide, E., Ducea, M., Mosenfelder, J., 2005. Discrete ultrahigh-pressure domains in the Western Gneiss Region, Norway: implications for formation and exhumation. J. Metamorph. Geol. 23, 45–61.
Rubatto, D., 2002. Zircon trace element geochemistry: partitioning with garnet and the link between U–Pb ages and metamorphism. Chem. Geol. 184, 123–138.
Schouenborg, B.E., 1988. U/Pb zircon dating of Caledonian cover rocks and cover-basement contacts, northern Vestranden, central Norway. Nor. Geol. Tidsskr. 68, 75–87.
Seydoux-Guillaume, A.M., Paquette, J.L., Wiedenbeck, M., Montel, J.M., Heinrich, W., 2002. Experimental resetting of the U–Th–Pb systems in monazite. Chem. Geol. 191, 165–181.
Size, W.B., 1979. Petrology, geochemistry and genesis of the type area trondhjemite in the Trondheim Region, central Norwegian Caledonides. Norges Geol. Unders. Bull. 351, 51–76.
Smith, D.C., 1984. Coesite in clinopyroxene in the Caledonides and its implications for geodynamics. Nature 310, 641–644.
Spencer, K.J., Hacker, B.R., Kylander-Clark, A.R.C., Andersen, T.B., Cottle, J.M., Stearns, M.A., Poletti, J.E., Seward, G.G.E., 2013. Campaign-style titanite U–Pb dating by laser-ablation ICP: implications for crustal flow, phase transformations and titanite closure. Chem. Geol. 341, 84–101.
Suzuki, K., Adachi, M., Tanaka, T., 1991. Middle Precambrian provenance of Jurassic sandstone in the Mino Terrane, central Japan: Th–U-total Pb evidence from an electron microprobe monazite study. Sediment. Geol. 75, 141–147.
Stacey, J.S., Kramers, J.D., 1975. Approximation of terrestrial lead isotope evolution by a two-stage model. Earth Planet. Sci. Lett. 26, 207–221.
Swensson, E., Andersen, T.B., 1991. Contact relationships between the Askvoll group and the basement gneisses of the Western Gneiss Region (WGR), Sunnfjord, Western Norway. Nor. Geol. Tidsskr. 71, 15–27.
Tera, F., Wasserburg, G.J., 1972. U-Th-Pb systematics in three Apollo 14 basalts and the problem of initial Pb in lunar rocks. Earth Planet. Sci. Lett. 14, 281–304.
Terry, M.P., Robinson, P., Ravna, E.J.K., 2000. Kyanite eclogite thermobarometry and evidence for thrusting of UHP over HP metamorphic rocks, Nordøyane, Western Gneiss Region, Norway. Am. Mineral. 85, 1637–1650.
Tillung, M., 1999. Structural and Metamorphic Development of the Hyllestad–Lifjorden Area, Western Norway. University of Bergen, Norway (Cand. Scient. thesis, 264 pp.).
Tomascak, P.B., Krogstad, E.J., Walker, R.J., 1996. U–Pb monazite geochronology of granitic rocks from Maine: implications for Late Paleozoic tectonics in the northern Appalachians. J. Geol. 104, 185–195.
Tucker, R.D., Råheim, A., Krogh, T.E., Corfu, F., 1987. Uranium–lead zircon and titanite ages from the northern portion of the Western Gneiss Region, south-central Norway. Earth Planet. Sci. Lett. 81, 203–211.
Tucker, R.D., Krogh, T.E., Råheim, A., 1990. Proterozoic evolution and age–province boundaries in the central part of the Western Gneiss region, Norway: results of U–Pb dating of accessory minerals from Trondheimsfjord to Geiranger. In: Gower, C.F., Rivers, T., Ryan, B. (Eds.), GAC Special Paper. Mid-Proterozoic Laurentia–Baltica vol. 38. Geological Association of Canada, St. John's (Newfoundland), pp. 149–173.
Tucker, R.D., Robinson, P., Solli, A., Gee, D.G., Thorsnes, T., Krogh, T.E., Nordgulen, Ø., Bickford, M.E., 2004. Thrusting and extension in the Scandian hinterland, Norway: New U–Pb ages and tectonostratigraphic evidence. Am. J. Sci. 304, 477–532.
Vrijmoed, J.C., Austrheim, H., John, T., Podladchikov, Y.Y., Anonymous, 2008. Metasomatism of the UHP Svartberget olivine–websterite body in the Western Gneiss Complex, Norway. Geochim. Cosmochim. Acta 72, A989.
Walsh, E.O., Hacker, B.R., 2004. The fate of subducted continental margins: two-stage exhumation of the high-pressure to ultrahigh-pressure Western Gneiss complex, Norway. J. Metamorph. Geol. 22, 671–689.
Walsh, E.O., Hacker, B.R., Grove, M., Gans, P.B., Gehrels, G., 2007. Timing the exhumation of (ultra)high-pressure rocks across the Western Gneiss Region, Norway. Geol. Soc. Am. Bull. 119, 289–301.
Walsh, E.O., Hacker, B.R., Andersen, T.B., Kylander-Clark, A.R.C., Johnston, S., Peterman, E., Young, D., 2013. Late exhumation of the ultrahigh-pressure Western Gneiss Region: structural geology and structural petrology. Tectonophysics 608, 1159–1179.
Yakymchuk, C., Brown, M., 2014. Behavior of zircon and monazite during crustal melting. J. Geol. Soc. Lond. 171, 465–479.
Young, D.J., Hacker, B.R., Andersen, T.B., Corfu, F., Gehrels, G.E., Grove, M., 2007. Amphibolite to ultrahigh-pressure transition in western Norway: implications for exhumation tectonics. Tectonics 26, TC1007. http://dx.doi.org/10.1029/2004TC001781.
Young, D.J., Hacker, B.R., Andersen, T.B., Gans, P.B., 2011. Structure and $^{40}Ar/^{39}Ar$ thermochronology of an ultrahigh-pressure transition in Western Norway. J. Geol. Soc. Lond. 168, 887–898.